The Astrophysical Journal, 710:1557–1577, 2010 February 20 doi:10.1088/0004-637X/710/2/1557

THE WEAK *s*-PROCESS IN MASSIVE STARS AND ITS DEPENDENCE ON THE NEUTRON CAPTURE CROSS SECTIONS

M. Pignatari[1,2,3], R. Gallino[4], M. Heil[5], M. Wiescher[2], F. Käppeler[6], F. Herwig[1], and S. Bisterzo[4]
[1] Department of Physics & Astronomy, University of Victoria, Victoria, BC V8P5C2 Canada
[2] Joint Institute for Nuclear Astrophysics, University of Notre Dame, Notre Dame, IN 46556, USA
[3] TRIUMF, 4004 Wesbrook Mall, Vancouver, BC V6T2A3, Canada; marcop@uvic.ca
[4] Dipartimento di Fisica Generale, Universitá di Torino, Via Pietro Giuria 1, Torino 10125, Italy
[5] Gesellschaft für Schwerionenforschung (GSI), D-64291 Darmstadt, Germany
[6] Forschungszentrum Karlsruhe, Institut für Kernphysik, Postfach 3640, 76021 Karlsruhe, Germany
Received 2009 December 5; accepted 2010 January 7; published 2010 February 1

ABSTRACT

The slow neutron capture process in massive stars (weak *s* process) produces most of the *s*-process isotopes between iron and strontium. Neutrons are provided by the ^{22}Ne(α,n)^{25}Mg reaction, which is activated at the end of the convective He-burning core and in the subsequent convective C-burning shell. The *s*-process-rich material in the supernova ejecta carries the signature of these two phases. In the past years, new measurements of neutron capture cross sections of isotopes beyond iron significantly changed the predicted weak *s*-process distribution. The reason is that the variation of the Maxwellian-averaged cross sections (MACS) is propagated to heavier isotopes along the *s* path. In the light of these results, we present updated nucleosynthesis calculations for a 25 $M_{\odot}$ star of Population I (solar metallicity) in convective He-burning core and convective C-burning shell conditions. In comparison with previous simulations based on the Bao et al. compilation, the new measurement of neutron capture cross sections leads to an increase of *s*-process yields from nickel up to selenium. The variation of the cross section of one isotope along the *s*-process path is propagated to heavier isotopes, where the propagation efficiency is higher for low cross sections. New ^{74}Ge, ^{75}As, and ^{78}Se MACS result in a higher production of germanium, arsenic, and selenium, thereby reducing the *s*-process yields of heavier elements by propagation. Results are reported for the He core and for the C shell. In shell C-burning, the *s*-process nucleosynthesis is more uncertain than in the He core, due to higher MACS uncertainties at higher temperatures. We also analyze the impact of using the new lower solar abundances for CNO isotopes on the *s*-process predictions, where CNO is the source of ^{22}Ne, and we show that beyond Zn this is affecting the *s*-process yields more than nuclear or stellar model uncertainties considered in this paper. In particular, using the new updated initial composition, we obtain a high *s*-process production (overproduction higher than ^{16}O, $\sim$100) for Cu, Ga, Ge, and As. Using the older abundances by Anders & Grevesse, also Se, Br, Kr, and Rb are efficiently produced. Our results have important implications in explaining the origin of copper in the solar abundance distribution, pointing to a prevailing contribution from the weak *s*-process in agreement with spectroscopic observations and Galactic chemical evolution calculations. Because of the improvement due to the new MACS for nickel and copper isotopes, the nucleosynthesis of copper is less affected by nuclear uncertainties compared to heavier *s*-process elements. An experimental determination of the ^{63}Ni MACS is required for a further improvement of the abundance prediction of copper. The available spectroscopic observations of germanium and gallium in stars are also discussed, where most of the cosmic abundances of these elements derives from the *s*-process in massive stars.

Key words: nuclear reactions, nucleosynthesis, abundances – stars: abundances

1. INTRODUCTION

About half of the nuclei beyond iron in the solar system are produced by the *s*-process, the other half by the rapid neutron capture process (*r*-process), and a marginal contribution is provided by the so-called *p*-process (Burbidge et al. 1957). Most of the *s* elements between iron and strontium ($60 \lesssim A \lesssim 90$) are produced in massive stars (with initial mass $M > 8\,M_{\odot}$), forming the weak *s* component (Käppeler et al. 1989; Beer et al. 1992b, and references therein). For $A \gtrsim 90$, the *s* elements are produced in asymptotic giant branch (AGB) stars ($1.3\,M_{\odot} \lesssim M \lesssim 8\,M_{\odot}$) forming the main *s* component (e.g., Arlandini et al. 1999). Finally, about 50% of the solar ^{208}Pb is provided by AGB stars at low metallicity, forming the strong *s* component (Gallino et al. 1998). Starting from Galactical chemical evolution calculations and from spectroscopic observation evidences, Travaglio et al. (2004a) showed that the weak *s* component and the main *s* component do not fully reproduce the *s* abundances between strontium and barium, proposing the existence of a new unknown component called lighter element primary process (LEPP). The nature of such a component is still under debate, and different scenarios have been proposed as an astrophysical site of the LEPP, i.e., the *s*-process in fast rotating massive stars at low metallicity (Pignatari et al. 2008) and the incomplete α-rich freeze-out in core collapse supernovae (SNe) during the high-entropy neutrino winds from a forming neutron star (e.g., Kratz et al. 2008; Qian & Wasserburg 2008; Farouqi et al. 2009).

In massive stars, the main neutron source is provided by the ^{22}Ne(α,n)^{25}Mg reaction, activated at the end of the convective He-burning core (Peters 1968; Couch et al. 1974; Lamb et al. 1977; Prantzos et al. 1990; Raiteri et al. 1991b) and in the following convective C-burning shell (e.g., Raiteri et al. 1991a). The ^{22}Ne abundance available in the He core is produced from the initial CNO isotopes, which are converted to ^{14}N during the H-burning phase, and then to ^{22}Ne via

^{14}N(α,γ)^{18}F($\beta^+\nu$)^{18}O(α,γ)^{22}Ne during He-burning. Once the central temperature in the He core is higher than 2.5×10^8 K ($T_9 = 0.25$, where $T_9 = 10^9$ K), the ^{22}Ne(α,n)^{25}Mg starts to activate the *s*-process. At He exhaustion, not all the ^{22}Ne is consumed (e.g., Prantzos et al. 1990). The ^{22}Ne(α,n)^{25}Mg reaction is re-activated during C-burning, where the α-particles required to produce neutrons are provided by the ^{12}C(^{12}C,α)^{20}Ne reaction channel (e.g., Arnett & Truran 1969). Raiteri et al. (1991a) showed that *s* nucleosynthesis occurs during convective shell C-burning at a high neutron density and with a neutron exposure comparable with the one in the previous He-burning core. Stellar models providing the evolution of the star up to the final phases and the SN explosion confirm this scenario (e.g., Woosley & Weaver 1995; Limongi et al. 2000; Woosley et al. 2002; The et al. 2007).

C-burning nucleosynthesis in the core is not relevant for the *s*-process, since the core material will collapse in the forming neutron star or black hole after the SN explosion. For instance, in a 25 $M_\odot$ star the region between the center and about 2 $M_\odot$ (mass coordinate) contributes to the forming neutron star. The mass range $2\,M_\odot \lesssim M_r \lesssim 3$–$3.5\,M_\odot$ is affected by explosive nucleosynthesis, and the neutron capture yields at the end of the hydrostatic evolution of the star are destroyed by photodisintegration (e.g., Thielemann & Arnett 1985; Tur et al. 2009). The O-rich and *s*-process-rich material in the mass range 3–$3.5\,M_\odot \lesssim M_r \lesssim 6$–$6.5\,M_\odot$ is ejected almost unchanged by the SN explosion (e.g., Woosley et al. 2002). In this mass region, most of the material is exposed to C shell nucleosynthesis, which modifies the *s*-process signature of the He core. Indeed, the final *s*-process yields in a 25 $M_\odot$ star are strongly affected by the C shell contribution. The rest of the mass (about 0.5–1 $M_\odot$ beyond the convective C shell) is a remnant of core He-burning, unchanged by following hydrostatic evolutionary phases. Finally, about 1.5 $M_\odot$ in the mass range $M_r \sim 6.5$–$8\,M_\odot$ is processed by convective shell He-burning (Woosley et al. 2002). According to different stellar models, the *s*-process in the He shell may be as efficient as in the He core (e.g., Woosley et al. 2002) or only marginally activated (e.g., Limongi et al. 2000), depending on the temperature at the bottom of the shell and on the corresponding ^{22}Ne(α,n)^{25}Mg efficiency. Subsequently, the He shell material is further processed during the SN explosion. Indeed, a significant amount of ^{22}Ne is still present at the shock wave passage, and the high neutron flow generated by the ^{22}Ne(α,n)^{25}Mg can significantly modify the pre-SN abundance signature in this small region (e.g., Woosley & Weaver 1995; Meyer et al. 2000). For these reasons, in the following analysis we will not consider the He shell contribution, but focus our attention on the He core and on the C shell.

Raiteri et al. (1991a, 1991b, 1992, 1993) and Käppeler et al. (1994) analyzed the *s*-process in massive stars, both in the He core and in the C shell, for different masses and metallicities. Meanwhile, a number of key reactions for the *s*-process have been updated. This list includes neutron capture cross sections between iron and strontium, reported in the compilation of Bao et al. (2000) and in further updates (KADoNIS; Dillmann et al. 2006), and in recent experimental works, i.e., by Alpizar-Vicente et al. (2008), Heil et al. (2008a, 2008b). The propagation effect of neutron capture cross sections on the *s*-process production of heavier isotopes was first underlined by Nassar et al. (2005) in the case of ^{62}Ni. This effect is observed for a large sample of cross sections between iron and strontium (Heil et al. 2008b). In the light of an updated nuclear network, using the same models as Raiteri et al. (1991a, 1991b), we present new *s*-process calculations in a 25 $M_\odot$ star at solar metallicity for both the convective He core and the subsequent convective C shell. In Section 2, we describe the main features of the post-processing models and of the nuclear network used in the calculations. The *s*-process calculations are presented in Section 3 for the He core and in Section 4 for the C shell. In Section 5, we analyze the *s*-process dependence on the neutron capture network, also including other important uncertainties in the analysis. In Section 6, we discuss the spectroscopic observations of light trans-iron elements copper, gallium, zinc, and germanium, where our calculations help explaining their astrophysical origin. In Section 7, the weak *s*-process production of ^{36}S and ^{80}Kr is briefly discussed. Finally, in Section 8, the main conclusions and final remarks are presented.

2. NUCLEAR NETWORK

The full network used in the present calculations includes all the isotopes relevant for *s*-process nucleosynthesis between H and Bi, but we restrict our analysis to the mass region below ^{100}Mo (Table 1), since the weak *s*-process contribution to isotopes heavier than the Sr–Y–Zr peak is marginal (e.g., Raiteri et al. 1991a). The α-capture and the *p*-capture reaction network is presented in Table 2. The important ^{22}Ne(α,n)^{25}Mg and ^{22}Ne(α,γ)^{26}Mg rates used in the present work are given in Table 3 compared to other references. The (n,γ) cross sections of stable isotopes are mainly provided by the Bao et al. (2000) compilation. More recent neutron capture rates are listed in Table 4 (see e.g., KADoNIS). The (n,γ) cross sections of unstable isotopes not included in Bao et al. (2000) or KADoNIS are from Rauscher & Thielemann (2000). The (n,α) and (n,p) reactions included in the nuclear network are listed in Table 5. The β-decay rates are adopted from Fuller et al. (1985) for $A < 45$, from Langanke & Martínez-Pinedo (2000) for $45 < A < 65$ and from Takahashi & Yokoi (1987) for the heavier isotopes. In this last case, for C-burning temperatures the β-decay rates have been extrapolated out of Takahashi & Yokoi (1987) tables, according to Neuberger (1991; see also Raiteri et al. 1993 for more details). The only exceptions of the recipe above are ^{79}Se, given by Klay & Käppeler (1988) instead of Takahashi & Yokoi (1987), and ^{85}Kr in He-burning conditions, which are important branching points along the *s*-process path. ^{85}Kr is an unstable isotope, characterized by a ground state, ^{85}Kr^{g} ($t_{1/2} = 10.76$ yr), and an isomeric state, ^{85}Kr^{m} ($t_{1/2} = 4.48$ hr). About 50% of the neutron capture on ^{84}Kr feeds ^{85}Kr^{m} (Bao et al. 2000). According to Ward et al. (1976), for $T_9 \lesssim 0.3$ the two states ^{85}Kr^{g} and ^{85}Kr^{m} are not thermalized and have to be treated as two separate nuclear species. The ground state and the isomer decay with their terrestrial rates, where 20% of ^{85}Kr^{m} decays via internal transition to the ground state, and the remaining 80% β^--decay to ^{85}Rb (see Käppeler et al. 1989). For unstable isotopes with $A > 65$ not included in Takahashi & Yokoi (1987), we use terrestrial β-decay rates. Such approximation has a minor effect on the *s*-process calculations, because it refers to unstable isotopes that are not produced in He burning conditions, or only marginally produced at the neutron densities typical of C burning.

The ^{12}C + ^{12}C total rate during C-burning is that of Caughlan & Fowler (1988), where the two reaction channels

^{12}C + ^{12}C $\rightarrow$ ^{20}Ne + ^{4}He ($Q = +4.616$ MeV)

^{12}C + ^{12}C $\rightarrow$ ^{23}Na + p ($Q = +2.238$ MeV)

have probabilities $\beta_\alpha = 0.65$ and $\beta_p = 0.35$ (Aguilera et al. 2006). For the third channel, ^{12}C(^{12}C,n)^{23}Mg, which is 2 orders

Table 1
Isotopic Network Adopted in the Calculations

Element	A_{min}	A_{max}	Element	A_{min}	A_{max}
H	1	1	Mn	55	56
He	4	4	Fe	54	61
C	12	14	Co	59	62
N	13	15	Ni	58	66
O	16	18	Cu	63	67
F	17	19	Zn	64	72
Ne	20	22	Ga	69	74
Na	21	24	Ge	70	78
Mg	24	28	As	75	79
Al	25	27	Se	76	82
Si	28	32	Br	79	84
P	31	33	Kr	80	88
S	32	38	Rb	85	89
Cl	35	39	Sr	86	93
Ar	36	44	Y	89	95
K	39	45	Zr	90	97
Ca	40	49	Nb	93	98
Sc	45	49	Mo	92	102
Ti	46	51			
V	51	51			
Cr	50	56			

Table 2
Charged Particle Network Adopted for the *s*-process Calculations in the Convective He-burning Core and in the Convective C-burning Shell

α-Captures	Reference	p-Captures	Reference
$^{12}C(\alpha,\gamma)^{16}O$	CFHZ85	$^{12}C(p,\gamma)^{13}N$	CF88
$^{13}C(\alpha,n)^{16}O$	CF88	$^{13}C(p,\gamma)^{14}N$	CF88
$^{14}C(\alpha,\gamma)^{18}O$	CF88	$^{14}C(p,\gamma)^{15}N$	CF88
$^{14}C(\alpha,n)^{17}O$	Schatz et al. (1993)	$^{14}C(p,n)^{14}N$	CF88
$^{14}N(\alpha,\gamma)^{18}F$	NACRE	$^{13}N(p,\gamma)^{14}O$	NACRE
$^{15}N(\alpha,\gamma)^{19}F$	NACRE	$^{14}N(p,\gamma)^{15}O$	NACRE
$^{16}O(\alpha,\gamma)^{20}Ne$	CF88	$^{15}N(p,\gamma)^{16}O$	NACRE
$^{17}O(\alpha,\gamma)^{21}Ne$	CF88	$^{15}N(p,\alpha)^{12}C$	NACRE
$^{17}O(\alpha,n)^{20}Ne$	CF88	$^{16}O(p,\gamma)^{17}F$	CF88
$^{18}O(\alpha,\gamma)^{22}Ne$	NACRE	$^{17}O(p,\gamma)^{18}F$	NACRE
$^{18}O(\alpha,n)^{21}Ne$	NACRE	$^{17}O(p,\alpha)^{14}N$	NACRE
$^{18}F(\alpha,p)^{21}Ne$	Wagoner (1969)	$^{18}O(p,\gamma)^{19}F$	NACRE
$^{19}F(\alpha,p)^{22}Ne$	CF88	$^{18}O(p,\alpha)^{15}N$	NACRE
$^{20}Ne(\alpha,\gamma)^{24}Mg$	NACRE	$^{18}F(p,\gamma)^{19}Ne$	Utku et al. (1998)
$^{21}Ne(\alpha,\gamma)^{25}Mg$	NACRE	$^{18}F(p,\alpha)^{15}O$	Utku et al. (1998)
$^{21}Ne(\alpha,n)^{24}Mg$	NACRE	$^{19}F(p,\gamma)^{20}Ne$	NACRE
$^{22}Ne(\alpha,\gamma)^{26}Mg$	Karakas et al. (2006)	$^{19}F(p,\alpha)^{16}O$	NACRE
$^{22}Ne(\alpha,n)^{25}Mg$	Jaeger et al. (2001)	$^{20}Ne(p,\gamma)^{21}Na$	CF88
$^{22}Na(\alpha,p)^{25}Mg$	NETGEN	$^{21}Ne(p,\gamma)^{22}Na$	NACRE
$^{23}Na(\alpha,\gamma)^{27}Al$	NETGEN	$^{22}Ne(p,\gamma)^{23}Na$	NACRE
$^{23}Na(\alpha,p)^{26}Mg$	NETGEN	$^{22}Na(p,\gamma)^{23}Mg$	NACRE
$^{24}Mg(\alpha,\gamma)^{28}Si$	CF88	$^{23}Na(p,\gamma)^{24}Mg$	NACRE
$^{24}Mg(\alpha,p)^{27}Al$	NACRE	$^{23}Na(p,\alpha)^{20}Ne$	NACRE
$^{25}Mg(\alpha,\gamma)^{29}Si$	CF88	$^{24}Mg(p,\gamma)^{25}Al$	NACRE
$^{25}Mg(\alpha,n)^{28}Si$	NACRE	$^{25}Mg(p,\gamma)^{26}Al$	NACRE
$^{25}Mg(\alpha,p)^{28}Al$	NETGEN	$^{26}Mg(p,\gamma)^{27}Al$	NACRE
$^{26}Mg(\alpha,\gamma)^{30}Si$	CF88	$^{26}Al(p,\gamma)^{27}Si$	NACRE
$^{26}Mg(\alpha,n)^{29}Si$	NACRE	$^{27}Al(p,\gamma)^{28}Si$	NACRE
$^{26}Al(\alpha,p)^{29}Si$	NETGEN	$^{28}Si(p,\gamma)^{29}P$	NACRE
$^{27}Al(\alpha,\gamma)^{31}P$	NETGEN	$^{29}Si(p,\gamma)^{30}P$	NACRE
$^{27}Al(\alpha,p)^{30}Si$	NETGEN	$^{30}Si(p,\gamma)^{30}P$	NACRE

References. (1) CFHZ85: Caughlan et al. 1985; (2) CF88: Caughlan & Fowler 1988; (3) NACRE: Angulo et al. 1999; (4) NETGEN: Aikawa et al. 2005.

Table 3
$^{22}Ne(\alpha,n)^{25}Mg$ and $^{22}Ne(\alpha,\gamma)^{26}Mg$ Rates from Different Sources ($cm^3\ mol^{-1}\ s^{-1}$) at He-burning and C-burning Temperatures

T_9	f	Käppeler et al. (1994)	NACRE	Jaeger et al. (2001)
		$^{22}Ne(\alpha,n)^{25}Mg$		
0.25	10^{-13}	$11.4^{20.5}_{2.40}$	$2.30^{314}_{1.82}$	$1.60^{2.6}_{1.48}$
0.30	10^{-11}	$9.09^{14.4}_{4.14}$	$4.06^{192}_{3.37}$	$2.69^{3.2}_{2.63}$
1.00	10^{-02}	$7.11^{9.25}_{5.27}$	$7.81^{8.91}_{6.99}$	$8.73^{9.59}_{7.86}$
1.25	1	...	$1.50^{1.68}_{1.33}$	$1.69^{1.99}_{1.46}$
		$^{22}Ne(\alpha,\gamma)^{26}Mg$		
				Karakas et al. (2006)
0.25	10^{-13}	$1.22^{2.80}_{0.47}$	$3.12^{30.1}_{0.34}$	$1.20^{2.05}_{0.88}$
0.30	10^{-11}	$1.22^{1.63}_{0.81}$	$2.56^{20.3}_{0.59}$	$1.71^{2.12}_{1.35}$
1.00	10^{-04}	$3.64^{4.03}_{3.22}$	$3.63^{7.95}_{2.73}$	$5.64^{6.69}_{4.62}$
1.25	10^{-03}	...	$2.41^{4.02}_{1.81}$	$3.42^{3.94}_{2.86}$

Notes. The rates used in the present work are listed in Column 5. Each entry must be multiplied by the factor f to obtain the correct values.

Table 4
Recent (n,γ) Cross Sections not Included in Bao et al. (2000)

(n,γ) Reaction	Reference
$^{17}O(n,\gamma)^{18}O$	Wagoner (1969)
$^{21}Ne(n,\gamma)^{22}Ne$	Heil et al. (2005)
$^{22}Ne(n,\gamma)^{23}Ne$	Beer et al. (2002)
$^{28}Si(n,\gamma)^{29}Si$	Guber et al. (2003)
$^{29}Si(n,\gamma)^{30}Si$	Guber et al. (2003)
$^{30}Si(n,\gamma)^{31}Si$	Guber et al. (2003)
$^{45}Sc(n,\gamma)^{46}Sc$	Heil et al. (2009)
$^{58}Fe(n,\gamma)^{59}Fe$	Heil et al. (2008b)
$^{54}Fe(n,\gamma)^{55}Fe$	Coquard et al. (2006)
$^{59}Co(n,\gamma)^{60}Co$	Heil et al. (2008b)
$^{58}Ni(n,\gamma)^{59}Ni$	I. Dillmann 2009, private communication
$^{60}Ni(n,\gamma)^{61}Ni$	Corvi et al. (2002)
$^{62}Ni(n,\gamma)^{63}Ni$	Alpizar-Vicente et al. (2008)
$^{64}Ni(n,\gamma)^{65}Ni$	Heil et al. (2008b)
$^{63}Cu(n,\gamma)^{64}Cu$	Heil et al. (2008b)
$^{65}Cu(n,\gamma)^{66}Cu$	Heil et al. (2008b)
$^{74}Ge(n,\gamma)^{75}Ge$	Marganiec et al. (2009)
$^{76}Ge(n,\gamma)^{77}Ge$	Marganiec et al. (2009)
$^{75}As(n,\gamma)^{76}As$	Marganiec et al. (2009)
$^{78}Se(n,\gamma)^{79}Se$	Dillmann et al. (2006)
$^{79}Br(n,\gamma)^{80}Br$	Heil et al. (2008a)
$^{81}Br(n,\gamma)^{82}Br$	Heil et al. (2008a)
$^{80}Kr(n,\gamma)^{81}Kr$	Mutti et al. (2005)
$^{82}Kr(n,\gamma)^{83}Kr$	Mutti et al. (2005)
$^{83}Kr(n,\gamma)^{84}Kr$	Mutti et al. (2005)
$^{84}Kr(n,\gamma)^{85}Kr$	Mutti et al. (2005)
$^{86}Kr(n,\gamma)^{87}Kr$	Mutti et al. (2005)
$^{85}Rb(n,\gamma)^{86}Rb$	Heil et al. (2008a)
$^{87}Rb(n,\gamma)^{88}Rb$	Heil et al. (2008a)

of magnitude lower in strength, we use the β_n probability from Dayras et al. (1977; e.g., $\beta_n \sim 10^{-3}$ at $T_9 \sim 1$).

3. CONVECTIVE CORE He-BURNING

In this section, we present *s*-process calculations in the convective He-burning core of a 25 $M_\odot$ stellar model at [Fe/H] = 0. The computational method used in the post-processing calculations is described in Busso & Gallino (1985) and Raiteri et al. (1991b). The stellar structure is provided by the

Table 5
(n,p) and (n,α) Rates Used in the Present Calculations

(n,p)	Reference	(n,α)	Reference
^{13}N(n,p)^{13}C	NACRE	^{17}O(n,α)^{14}C	Schatz et al. (1993)
^{14}N(n,p)^{14}C	Koehler & O'Brien (1989)	^{18}F(n,α)^{15}N	NETGEN
^{18}F(n,p)^{18}O	NETGEN	^{22}Na(n,α)^{19}F	RT2000
^{22}Na(n,p)^{22}Ne	RT2000	^{26}Al(n,α)^{23}Na	Skelton et al. (1987)
^{26}Al(n,p)^{26}Mg	Koehler et al. (1997)	^{33}S(n,α)^{30}Si	RT2000
^{32}P(n,p)^{32}Si	RT2000	^{37}Ar(n,α)^{34}S	Goeminne et al. (2000)
^{36}Cl(n,p)^{36}S	de Smet et al. (2005)	^{39}Ar(n,α)^{36}S	RT2000
^{37}Ar(n,p)^{37}Cl	Goeminne et al. (2000)	^{40}K(n,α)^{37}Cl	RT2000
^{40}K(n,p)^{40}Ar	RT2000	^{41}Ca(n,α)^{38}Ar	Wagemans et al. (1995)
^{41}Ca(n,p)^{41}K	Wagemans et al. (1995)	^{59}Ni(n,α)^{56}Fe	RT2000
^{46}Sc(n,p)^{46}Ca	RT2000	^{65}Zn(n,α)^{62}Ni	RT2000
^{55}Fe(n,p)^{55}Mn	RT2000	^{71}Ge(n,α)^{68}Zn	RT2000
^{59}Ni(n,p)^{59}Co	RT2000		
^{64}Cu(n,p)^{64}Ni	RT2000		
^{65}Zn(n,p)^{65}Cu	RT2000		
^{70}Ga(n,p)^{70}Zn	RT2000		
^{80}Br(n,p)^{80}Se	RT2000		

References. (1) NACRE: Angulo et al. (1999); (2) NETGEN: Aikawa et al. (2005); (3) RT2000: Rauscher & Thielemann (2000).

FRANEC code (see Chieffi & Straniero 1989; Käppeler et al. 1994, for more details). The set of initial abundances is from Anders & Grevesse (1989).

In Table 6, the main *s*-process parameters are reported at He exhaustion for two models: Model 1 and Model 2. Model 1 (standard case) is calculated using the network described in the previous section, whereas Model 2 has been calculated using the older ^{22}Ne + α reaction rates by (Angulo et al. 1999, Nuclear Astrophysics Compilation of Reaction Rates (NACRE) compilation). The latter rates are higher at He-burning temperatures (Table 3), causing a more efficient burning of ^{22}Ne. The effect of a higher ^{22}Ne(α,n)^{25}Mg rate is partially reduced by the ^{22}Ne(α,γ)^{26}Mg rate, which is in competition with the neutron channel. The corresponding results from Raiteri et al. (1991b) are included in Table 6 for comparison. Those calculations were based on the same stellar model structure used for this work, and on an older nuclear reaction network. Raiteri et al. used the ^{22}Ne + α rates by Caughlan & Fowler (1988), and the ^{16}O(n,γ)^{17}O Maxwellian-averaged cross sections (MACS) by (Beer et al. 1992a, about a factor of 40 lower than Bao et al. 2000). See below in the text where more cases are discussed. As a result, in Model 1 the neutron exposure and the neutron capture per iron seed are a factor of 1.05 and 1.14 lower than in Raiteri et al. (1991b), pointing to a less efficient *s*-process. With respect to Raiteri et al. (1991b), Model 2 shows a very similar neutron exposure, a higher neutron capture per iron seed, and a higher amount of ^{22}Ne left at He exhaustion.

In Table 7, isotope overabundances ($X_i/X_\odot$) in the He core material are reported at He exhaustion up to ^{100}Mo for the cases presented in Table 6. Comparing the light isotope distributions, ^{31}P and ^{36}S are underproduced in both Model 1 and Model 2 with respect to Raiteri et al. (1991b). The ^{30}Si(n,γ)^{31}Si(β^-)^{31}P MACS by Guber et al. (2003) reduces by a factor of 3.83, a previous measurement (see Bao et al. 2000), affecting the ^{31}P nucleosynthesis in the He core. Concerning ^{36}S, we refer to Section 7.1 for a more detailed discussion. Beyond iron, in Model 1 and Model 2 the *s*-process is less efficient with respect to Raiteri et al. (1991b). The average overabundance of the six *s*-only isotopes between iron and strontium (^{70}Ge, ^{76}Se, ^{80,82}Kr, and ^{86,87}Sr) is 126 and 168 for Model 1 and Model 2, compared to 239 for Raiteri et al. (1991b). These differences are due to different nuclear reaction rates used in the calculations. The evolution of a sample of light and heavy isotopes calculated with Model 1 is illustrated in Figure 1 for the He-burning core. Panel (a) shows the temporal evolution of ^{4}He and of ^{12}C and ^{16}O, the most abundant products in core He-burning. The neutron source reaction ^{22}Ne(α,n)^{25}Mg starts to burn close to He exhaustion, in competition with the ^{12}C(α,γ)^{16}O reaction (e.g., Käppeler et al. 1994). The ^{25}Mg and ^{26}Mg abundances are produced by α-capture reactions on ^{22}Ne, where ^{25}Mg is the strongest neutron poison for the weak *s*-process. About 20% of the neutrons released are captured by ^{56}Fe (initial mass fraction of ^{56}Fe is 1.169×10^{-3}; Anders & Grevesse 1989), feeding *s*-process nucleosynthesis of heavier elements (Figure 1(b)). The evolution of the *s*-only isotopes between Fe and Sr (^{70}Ge, ^{76}Se, ^{80,82}Kr, and ^{86,87}Sr) is summarized in panel (c), showing that their overabundances are varying from 69 for ^{87}Sr to 169 for ^{80}Kr. In panel (c), we also report the evolution of ^{76}Ge and ^{88}Sr: ^{76}Ge is considered an *r*-only isotope (e.g., Arlandini et al. 1999, and reference therein), and it is preceded by unstable ^{75}Ge with a short halflife ($t_{1/2}$ = 83 minutes); ^{88}Sr is neutron magic (N = 50, with a low MACS (30 keV) = 6.2 ± 0.3 mbarn; Bao et al. 2000), and is accumulated during the *s* flow. Beyond

Table 6
Neutron Exposure τ, Mean Neutron Density $\bar{n}_n$, Central Peak Neutron Density n_n^{peak}, n_c Parameter, and the Amount of ^{22}Ne at Core He Exhaustion of a 25 $M_\odot$ Star and [Fe/H] = 0

Parameter	This Work		Ra91a
	Model 1	Model 2	
τ (mb^{-1})	0.197	0.209	0.206
$\bar{n}_n$ (10^6 cm^{-3})	1.14	1.01	0.68
n_n^{peak} (10^7 cm^{-3})	3.22	2.88	1.80
n_c	4.95	5.35	5.66
X_{22} (10^{-2})	1.14	0.70	0.96

Notes. Model 1 is our standard case using the best nuclear reaction network set. The corresponding results obtained with ^{22}Ne + α rates of Angulo et al. 1999 (Model 2) and of Raiteri et al. 1991b (Ra91a) are given for comparison.

Table 7
Production Factors Normalized to Solar (Anders & Grevesse 1989) at Core He Exhaustion of a 25 $M_{\odot}$ Star at [Fe/H] = 0

X_i	This Work		Ra91a	X_i	This Work		Ra91a
	Model 1	Model 2			Model 1	Model 2	
C 12 ...	63.7	64.2	57.0	Ar 36 ...	0.2	0.1	...
C 13 ...	0.0	0.0	...	Ar 38 ...	3.4	3.4	...
N 14 ...	0.0	0.0	...	Ar 40 ...	44.1	46.8	47.9
N 15 ...	0.0	0.0	...	K 39 ...	2.6	2.7	...
O 16 ...	82.5	82.2	84.9	K 40 ...	248	260	291.7
O 17 ...	3.6	3.0	...	K 41 ...	9.9	10.1	...
O 18 ...	0.0	0.0	...	Ca 40 ...	0.2	0.2	...
F 19 ...	0.7	0.7	...	Ca 42 ...	9.0	9.1	...
Ne 20 ...	2.0	2.0	...	Ca 43 ...	11.9	12.1	...
Ne 21 ...	5.5	5.6	...	Ca 44 ...	3.2	3.3	...
Ne 22 (158)[a]	89.1	54.7	74.9	Ca 46 ...	0.3	0.3	...
Na 23 ...	7.6	6.9	...	Ca 48 ...	0.8	0.8	...
Mg 24 ...	0.9	0.9	...	Sc 45 ...	16.7	17.7	...
Mg 25 ...	64.6	69.3	76.6	Ti 46 ...	5.7	6.2	...
Mg 26 ...	78.7	142.2	96.6	Ti 47 ...	2.1	2.3	...
Al 27 ...	1.2	2.1	...	Ti 48 ...	0.3	0.3	...
Si 28 ...	0.8	0.9	...	Ti 49 ...	5.1	5.5	...
Si 29 ...	2.0	2.0	...	Ti 50 ...	19.1	20.0	15.9
Si 30 ...	10.9	11.2	...	V 51 ...	0.5	0.6	...
P 31 ...	9.9	10.8	28.2	Cr 52 ...	0.2	0.2	...
S 32 ...	0.5	0.4	...	Cr 53 ...	0.3	0.3	...
S 33 ...	1.1	1.1	...	Cr 54 ...	15.0	14.6	16.5
S 34 ...	1.5	1.5	...	Mn 55 ...	0.1	0.1	...
S 36 ...	28.5	29.2	85.5	Fe 54 ...	0.0	0.0	...
Cl 35 ...	0.2	0.2	...	Fe 56 ...	0.2	0.2	...
Cl 37 ...	64.4	64.8	65.8	Fe 57 ...	2.1	1.9	...
Fe 58 ...	82.2	77.2	84.2	Br 79 ...	15.6	21.3	36.6
Co 59 ...	31.4	29.9	35.9	Br 81 ...	15.4	21.1	...
Ni 58 ...	0.0	0.0	...	Kr 78 ...	0.0	0.0	...
Ni 60 ...	9.1	9.0	...	Kr 80 ...	169	232	480.7
Ni 61 ...	66.3	65.8	84.6	Kr 82 ...	79.1	108	210.3
Ni 62 ...	52.6	53.7	49.9	Kr 83 ...	25.9	35.5	63.0
Ni 64 ...	148	166	164.5	Kr 84 ...	22.0	29.9	52.6
Cu 63 ...	127	134	91.8	Kr 86 ...	0.7	0.8	...
Cu 65 ...	280	317	226.3	Rb 85 ...	14.8	20.0	28.6
Zn 64 ...	34.1	36.8	41.0	Rb 87 ...	0.8	0.8	...
Zn 66 ...	76.3	88.7	118.9	Sr 84 ...	0.0	0.0	...
Zn 67 ...	109	127	171.7	Sr 86 ...	79.9	107	147.3
Zn 68 ...	99.1	121	164.7	Sr 87 ...	68.8	91.4	129.2
Zn 70 ...	0.3	0.3	...	Sr 88 ...	21.5	26.8	34.8
Ga 69 ...	126	156	208.6	Y 89 ...	15.6	18.9	22.3
Ga 71 ...	147	187	263.9	Zr 90 ...	6.9	8.2	...
Ge 70 ...	154	193	253.7	Zr 91 ...	8.6	10.1	...
Ge 72 ...	88.0	114	190.7	Zr 92 ...	7.3	8.5	...
Ge 73 ...	82.4	107	128.8	Zr 94 ...	5.4	6.3	...
Ge 74 ...	71.0	94.2	99.3	Zr 96 ...	0.1	0.1	...
Ge 76 ...	0.0	0.0	...	Nb 93 ...	6.1	7.1	...
As 75 ...	45.3	60.2	59.6	Mo 92 ...	0.0	0.0	...
Se 74 ...	0.0	0.0	...	Mo 94 ...	0.0	0.0	...
Se 76 ...	99.4	133	212.2	Mo 95 ...	2.2	2.6	...
Se 77 ...	44.0	59.1	88.6	Mo 96 ...	5.0	5.8	...
Se 78 ...	67.4	91.7	108.9	Mo 97 ...	2.8	3.2	...
Se 80 ...	1.5	1.9	...	Mo 98 ...	3.4	4.0	...
Se 82 ...	0.1	0.1	...	Mo 100...	0.0	0.0	...

Notes. The corresponding results obtained with ^{22}Ne + α rates of Angulo et al. 1999 (Model 2) and of Raiteri et al. 1991b (Ra91a) are given for comparison.
[a] ^{22}Ne available when the *s* process starts.

^{88}Sr the weak *s*-process efficiency rapidly decreases (e.g., Raiteri et al. 1991b). Finally, the neutron density and the neutron capture per iron seed are plotted in panel (d). In particular, the neutron density increase is due to the growth of the central temperature near core He exhaustion, boosting the ^{22}Ne(α,n)^{25}Mg efficiency.

In Figure 2, the overabundances between ^{57}Fe and ^{100}Mo are plotted at He exhaustion relative to the ^{16}O overabundance

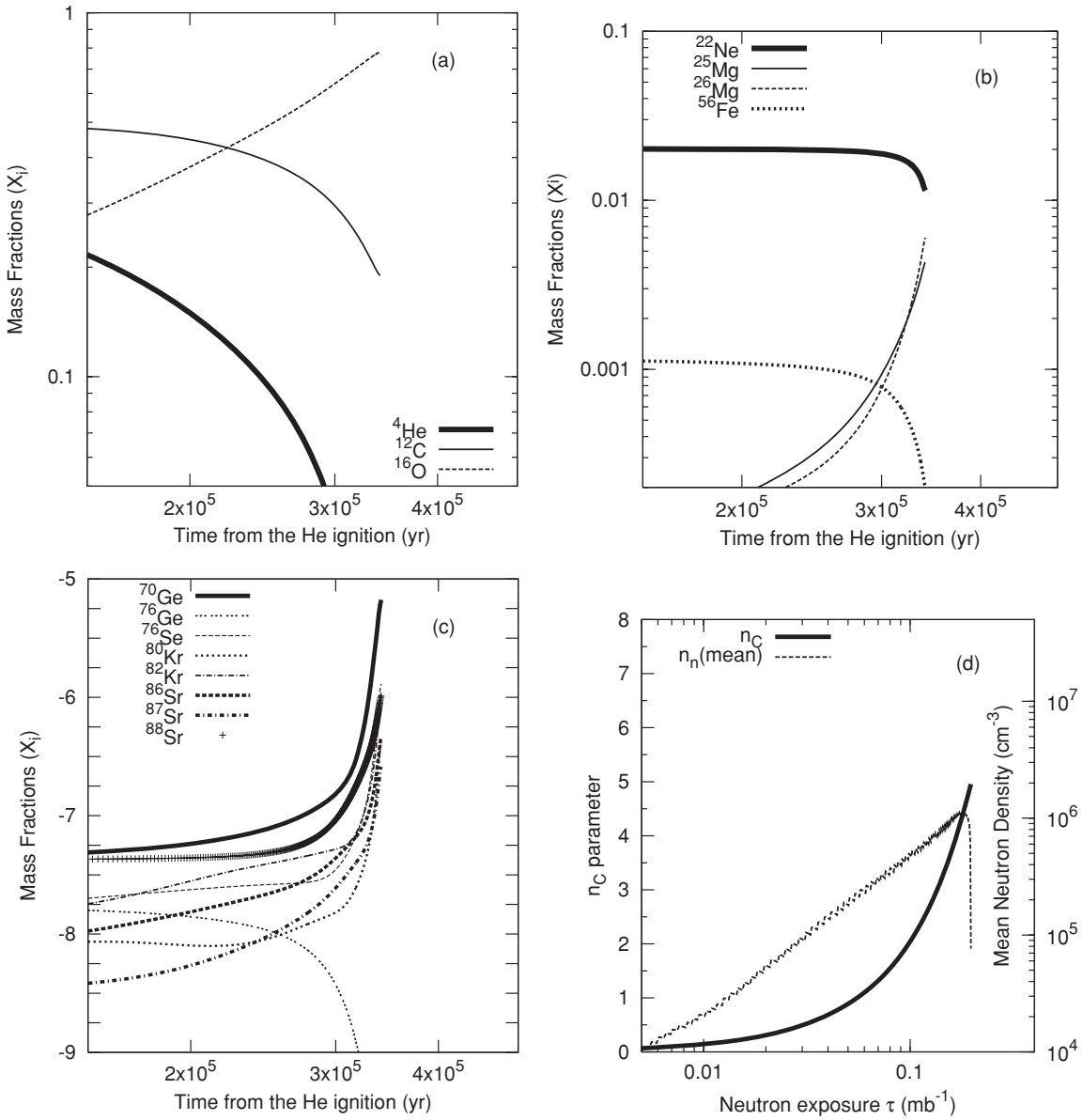

Figure 1. (a)–(c) Evolution of a sample of isotopes during core He-burning (25 $M_{\odot}$ and [Fe/H] = 0). (d) Evolution of the n_c parameter (number of neutrons captured per iron seed) and of the mean neutron density n_n(mean) vs. the neutron exposure τ.

as reference, because ^{16}O is primary[7] and the most abundant species, and all the cosmic ^{16}O is produced in massive stars. The lines ^{16}O×2 and ^{16}O/2 correspond to the ^{16}O overabundances multiplied and divided by a factor of 2. According to Tinsley (1980), at solar metallicity a pure secondary-like isotope is overproduced by a factor of 2 more than a pure primary-like isotope *if* they are fully synthesized by the same astrophysical source. Under the hypothesis that the *s*-process in massive stars is a pure secondary process, the *s*-only isotopes at solar metallicity should be overproduced by a factor of 2 compared to ^{16}O, and should lie on the line ^{16}O×2. Actually, the weak *s*-process is not a pure secondary-like process, since it depends on the initial mass and composition of the star at metallicity lower than solar (e.g., Prantzos et al. 1990; Raiteri et al. 1992; Baraffe et al. 1992). Furthermore, analyzing the *s*-process distribution between Fe and Sr in more detail, different *s* isotopes show a different metallicity dependence (e.g., Pignatari & Gallino 2008). Nevertheless, in first approximation isotopes receiving an important contribution from the weak *s*-process show an overabundance higher than ^{16}O.

In Figure 2, the overabundances higher than ^{16}O or at the same level are ^{58}Fe, ^{64}Ni, ^{63,65}Cu, ^{66,67,68}Zn, ^{69,71}Ga, ^{70,72,73}Ge, ^{76,78}Se, ^{80,82}Kr, and ^{86,87}Sr.

4. SHELL C-BURNING: *s*-PROCESS CALCULATIONS

Once He has been consumed in the convective core, temperature and density increase until C-burning is activated in the center. In particular, if the energy produced by ^{12}C + ^{12}C dominates over the energy lost by neutrinos, the C core becomes convective (El Eid et al. 2004). Once carbon is exhausted in the core, C-burning continues in one or more convective C shells, extending over the *s*-process-rich ashes of the previous convective He-burning core. During the C-burning phase, α-particles and protons are available at the same time. The α-particles are

[7] The production of primary (secondary) isotopes does not (does) depend on the initial metallicity of the star.

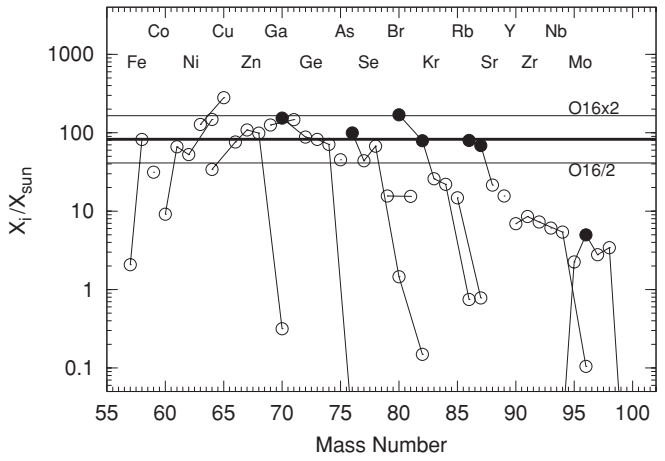

Figure 2. Overabundances between ^{57}Fe and ^{100}Mo at core He exhaustion for the 25 $M_\odot$ and [Fe/H] = 0 model. Full circles are the *s*-only isotopes, the other stable isotopes are reported with open circles. The thick line indicates the ^{16}O overabundance at He exhaustion. The initial solar composition is given by Anders & Grevesse (1989).

provided by the ^{12}C(^{12}C,α)^{20}Ne reaction. The strongest α-capture channels are ^{16}O(α,γ)^{20}Ne (where ^{16}O is the most abundant species), ^{20}Ne(α,γ)^{24}Mg and also ^{22}Ne(α,n)^{25}Mg, where the ^{22}Ne was left in the ashes of the previous convective He-burning core (Raiteri et al. 1991a).

Protons are provided by the ^{12}C(^{12}C,p)^{23}Na reaction. The most important p-capture channels are ^{23}Na(p,α)^{20}Ne, ^{22}Ne(p,γ)^{23}Na, ^{26}Mg(p,γ)^{27}Al, ^{17}O(p,α)^{14}N, and ^{25}Mg(p,γ)^{26}Al. ^{12}C(p,γ)^{13}N is the most efficient proton absorber under C-burning conditions, because of the high initial ^{12}C abundance and the high (p,γ) rate. For $T_9 \gtrsim 0.8$, however, protons captured by ^{12}C are immediately re-emitted and recycled by the inverse reaction ^{13}N(γ,p)^{12}C (Clayton 1968).

The ^{12}C(^{12}C,n)^{23}Mg reaction provides a marginal source of neutrons compared to ^{22}Ne(α,n)^{25}Mg at typical temperatures in the C shell (Dayras et al. 1977). The ^{12}C(^{12}C,n)^{23}Mg rate is highly uncertain, and it could be activated at higher temperatures if some residual carbon is left in more advanced evolutionary phases and/or in explosive C-burning conditions.

For a 25 $M_\odot$ stellar model, the material inside 3–3.5 $M_\odot$ in mass coordinate is further modified by explosive nucleosynthesis and the *s* yields are destroyed. In few cases (e.g., ^{80}Kr), *s* isotopes are produced again in significant amount by photodisintegration (e.g., Tur et al. 2009). On the other hand, the outer part of the C shell is ejected unchanged by explosive nucleosynthesis (e.g., Woosley et al. 2002). Therefore, the *s*-process contribution in this phase is crucial. Also for more massive stars (e.g., for 30 $M_\odot$) most of the *s*-process yields are modified by shell C-burning. However, the ^{22}Ne abundance left in the He core ashes decreases with increasing initial stellar mass, reducing the relative *s*-process efficiency in the C shell with respect to the He core (e.g., Prantzos et al. 1990; Käppeler et al. 1994). In stars with lower initial mass (as in a 15 $M_\odot$), only a small fraction of the ^{22}Ne abundance is burnt during core He-burning. However, the typical size of the convective C shell is smaller than in more massive stars, and most of the C shell material is processed by the SN explosion (e.g., Woosley & Weaver 1995; Limongi et al. 2000; Rauscher et al. 2002).

Raiteri et al. (1991a) simulated the C shell nucleosynthesis at constant temperature (T_9 = 1.05), based on Nomoto & Hashimoto (1988) models for a 25 $M_\odot$ star. Indeed, for most of the shell evolution, the temperature is constant or slowly growing because of the high temperature dependence of the ^{12}C + ^{12}C reaction ($\lambda_{^{12}C^{12}C} \propto T^{29}$; Woosley et al. 2002).

Shortly before the SN explosion thermal instabilities occur in O-burning layers, and temperature rapidly increases also in outer stellar material (Arnett 1974; Arnett & Wefel 1978). In recent calculations, Limongi et al. (2000) showed that in a 25 $M_\odot$ star in the last convective C shell the temperature rapidly increases from $T_9 = 1.07$ to $T_9 = 1.39$ at the bottom. According to Limongi et al. (2000), the C shell lasts 0.39 yr and the peak neutron density is a few times 10^{12} cm^{-3}. These results are supported by El Eid et al. (2004), but these authors find a slight temperature increase in the C shell also in the first phase. On the other hand, the *s*-process yields are not affected by such a temperature increase if convective shell C-burning is not active in the last days before the SN explosion. For instance, convective shell C-burning can be prohibited by stellar structure modifications due to O ignition in the core (e.g., Hirschi et al. 2004). In this case, the final *s*-process yields are not affected by a late temperature increase, and pre-SN convective C shell nucleosynthesis occurs only during the constant temperature phase (Raiteri et al. 1991a).

In this section, we present C shell *s*-process nucleosynthesis calculations using an updated nuclear network (Section 2). We also discuss the consequences of the last temperature peak on the *s*-process yields. Nucleosynthesis calculations for the C shell are performed with a single-zone post-processing code (e.g., Käppeler et al. 1994).

Full stellar model calculations are the best tool to provide more consistent weak *s*-process yields (e.g., The et al. 2007), and a single-zone model may seem to be a too simple approximation in this sense. Moreover, full stellar models are also able to directly take into account the explosive nucleosynthesis contribution to *s* isotopes (see, for example, Rauscher et al. 2002; Tur et al. 2009), that need to be consistently considered to provide weak *s* component predictions. Single-zone models are justified for the *s*-process analysis in the convective C shell making two assumptions. (1) During the C shell evolution the α and neutron density peaks are located in a small region close to the bottom of the shell where the maximum neutron exposure is reached. Above this region the neutron density and therefore the neutron capture timescale[8] rapidly decrease. Indeed, because of the steep temperature dependence of the neutron source reaction, the neutron capture nucleosynthesis is localized at the bottom of the convection zone. (2) The average convective turnover timescale in the C shell ($\sim$ hour) is generally faster than the nuclear timescale, causing a constant abundance distribution in the shell material of full 25 $M_\odot$ stellar models (e.g., Woosley & Weaver 1995; Limongi et al. 2000). Let us take as example critical reactions affecting the *s* nucleosynthesis of ^{80}Kr at typical temperature in the C shell ($\sim$ 90 keV). The timescale of ^{79}Se(n,γ)^{80}Se, ^{79}Se(β^-)^{79}Br, and ^{80}Kr(n,γ)^{81}Kr are about 2.5 hr, 0.4 yr, and 1.8 hr, respectively, assuming a neutron density of 10^{12} cm^{-3} that is reached in the final neutron burst. Therefore, in the final high temperature phase of the C shell the nuclear timescale is of the order of the convective turnover timescale. In these conditions, the one-zone model could not be fully realistic. The same is true for post-processing of full one-dimensional stellar model profiles that do not treat burning and mixing simultaneously. The mixing coefficients

[8] $\tau_n = \ln(2)/\lambda_n = \ln(2)/(\sigma_n \times v_T \times N_n \times 10^{-27})$ s, where σ_n is the neutron capture cross section in mbarn, v_T is the neutron thermal velocity ($\sim 4 \times 10^8$ cm s^{-1} at 90 keV), N_n is the neutron density, and 10^{-27} is a converting factor of mbarn in cm^{-2}.

Table 8
Neutron Exposure τ, Shell Peak Neutron Density n_n^{peak}, n_c Parameter, and the Amount of ^{12}C and ^{22}Ne are Reported for the C Shell Before the Final Temperature Increase and at the End

Parameter	Model 1		Model 2		Ra91b
	$T_9 = 1.05$	$T_9 = 1.40$	$T_9 = 1.05$	$T_9 = 1.40$	
τ(30 keV) (mb^{-1})	0.087	0.096	0.059	0.065	0.059
n_n^{peak} (10^{11} cm^{-3})	1.96	50.07	1.36	37.75	1.672
n_c	2.39	18.57	1.66	11.14	2.304
$X(^{12}C)$ ($\times 10^{-2}$)	6.34	5.01	6.38	5.03	
$X(^{22}Ne)$ ($\times 10^{-3}$)	0.61	0.12	0.37	0.08	

Note. The corresponding results obtained with $^{22}Ne + \alpha$ rates of Angulo et al. 1999 (Model 2) and of Raiteri et al. 1991a (Ra91b) are reported for comparison.

used in one-dimensional stellar evolution are usually derived from the mixing-length theory (MLT; Kippenhahn & Weigert 1990), which is only concerned with the properties averaged over long timescale (over many convective turnover timescales) and over large spatial scales (of the order $\alpha_{MLT} \times H_p$, where α_{MLT} is the mixing-length parameter and H_p is the pressure scale height). However, neutron densities $\gtrsim 10^{12}$ cm^{-3} in the C shell are reached only for a short time before the SN explosion, whereas in most of the C shell evolution neutron densities are $n_n \lesssim 10^{11}$ cm^{-3}. In this regime, the nuclear timescales are longer than the convective turnover timescale, and also assumption (2) is satisfied. A single-zone model may be calibrated on a full stellar model, providing *s*-process calculations in the C shell consistent with the original full stellar model (e.g., Raiteri et al. 1991a). For this reason, the one-zone model can correctly study and quantify the impact of nuclear uncertainties on the final *s*-process distribution, giving guidance and constraining indications for the *s*-process nucleosynthesis. In Section 8, we will come back to this point.

Our calculations start at C ignition, using as initial abundances those obtained at the core He exhaustion (Section 3, Table 7, Model 1 and Model 2), following the approach of Raiteri et al. (1991a). The C-burning temperature is $T_9 = 1.05$ during most of the shell evolution (~0.28 yr, when 2/3 of the initial ^{12}C is burned), and then increases in the last day up to $T_9 = 1.40$. A simple linear increase of temperature is applied in the simulations.

In Table 8, the main *s*-process parameters are listed at $T_9 = 1.05$ (0.28 yr, before the final T increase) and at $T_9 = 1.4$ (at the end of the C shell), using our standard $^{22}Ne + \alpha$ rates (Model 1, Columns 2 and 3), and the $^{22}Ne + \alpha$ rates of NACRE (Model 2, Columns 4 and 5). Column 6 contains the main *s*-process parameters from Raiteri et al. (1991a) for comparison. The neutron exposure τ is given at $kT = 30$ keV (where k is the Boltzmann constant and T is the temperature), for comparison with Table 6. In Table 9, the isotopic distribution is reported up to ^{100}Mo for both models at the two different phases (Columns 2, 3 and Columns 4, 5, respectively). The data of Raiteri et al. (1991a) are shown in Column 6 for comparison.

The *s*-process yields in Columns 2, 4, and 6 are the result of an initial neutron density peak ($n_n \sim 2 \times 10^{11}$ cm^{-3} in Model 1), followed by a rapid neutron freeze-out. On the other hand, the *s* yields in Columns 3, 5 have been also affected by a final neutron burst (~ few 10^{12} cm^{-3}), which is 1 order of magnitude higher than the first peak. Compared to Model 1, Model 2 is characterized by lower neutron exposure, neutron peak densities and neutron capture per iron seed (n_c) values, because the higher

Table 9
Production Factors Normalized to Solar (Anders & Grevesse 1989) for the C Shell Before and After the Final Temperature Increase

	Model 1		Model 2		Ra91b
X_i	$T_9 = 1.05$	$T_9 = 1.40$	$T_9 = 1.05$	$T_9 = 1.40$	
C 12	21.3	16.8	21.4	16.6	
C 13	0.0	0.0	0.0	0.0	
N 14	0.1	0.0	0.1	0.0	
N 15	0.1	0.0	0.1	0.0	
O 16	75.6	74.4	75.1	73.7	
O 17	4.3	0.0	2.7	0.0	
O 18	0.1	0.0	0.1	0.0	
F 19	0.2	0.1	0.1	0.1	
Ne 20	107	126	110	131	
Ne 21	179	90.7	114	58.1	
Ne 22	4.7	0.9	2.9	0.5	
Na 23	397	420	382	408	
Mg 24	15.4	28.5	15.3	29.6	
Mg 25	150	150	117	117	
Mg 26	86.4	87.0	92.7	88.7	
Al 27	96.6	102	140	145	
Si 28	2.2	3.0	2.5	3.3	
Si 29	8.7	15.4	9.1	16.7	
Si 30	16.9	17.9	17.3	18.4	
P 31	12.5	12.4	12.5	12.5	
S 32	0.4	0.3	0.4	0.4	
S 33	1.9	1.7	1.9	1.7	
S 34	1.8	1.8	1.7	1.7	
S 36	39.2	41.1	35.0	36.1	
Cl 35	0.5	0.5	0.4	0.4	
Cl 37	65.0	64.8	65.6	65.5	
Ar 36	0.1	0.1	0.1	0.1	
Ar 38	3.3	3.2	3.4	3.3	
Ar 40	124	137	93.3	101	
K 39	3.6	3.7	3.4	3.5	
K 40	107	99.8	137	130	
K 41	7.1	6.9	8.0	7.7	
Ca 40	0.1	0.1	0.1	0.1	
Ca 42	8.1	7.9	8.8	8.7	
Ca 43	15.9	15.6	16.3	16.2	
Ca 44	3.9	3.9	3.8	3.8	
Ca 46	480	505	282	299	
Ca 48	0.8	0.8	0.8	0.8	
Sc 45	22.1	22.7	21.5	22.0	
Ti 46	2.9	3.2	3.8	3.9	
Ti 47	2.7	2.7	3.1	3.1	
Ti 48	0.5	0.5	0.5	0.6	
Ti 49	6.3	6.5	6.2	6.4	
Ti 50	21.3	21.6	21.6	21.8	
V 51	1.1	1.1	1.0	1.0	
Cr 52	0.1	0.1	0.2	0.1	
Cr 53	0.4	0.4	0.4	0.4	
Cr 54	12.9	12.7	13.0	12.8	
Mn 55	0.1	0.1	0.1	0.1	
Fe 54	0.0	0.0	0.0	0.0	
Fe 56	0.1	0.1	0.1	0.1	
Fe 57	1.5	1.4	1.7	1.6	
Fe 58	51.4	48.8	55.5	53.4	56.7
Co 59	53.5	53.1	49.1	49.7	
Ni 58	0.0	0.0	0.0	0.0	
Ni 60	5.8	5.8	6.1	6.1	
Ni 61	55.8	54.0	59.2	57.2	
Ni 62	61.9	61.2	62.5	62.3	
Ni 64	232	242	221	227	
Cu 63	219	227	179	189	
Cu 65	185	181	224	216	
Zn 64	1.7	1.1	4.7	3.4	
Zn 66	81.9	76.7	107	101	

Table 9
(Continued)

	Model 1		Model 2		Ra91b
X_i	$T_9 = 1.05$	$T_9 = 1.40$	$T_9 = 1.05$	$T_9 = 1.40$	
Zn 67	212	200	272	261	
Zn 68	249	252	250	260	
Zn 70	31.4	136	21.7	85.2	
Ga 69	352	387	337	373	
Ga 71	425	442	364	401	
Ge 70	471	418	421	404	527.1
Ge 72	296	349	246	283	
Ge 73	458	509	381	411	
Ge 74	305	339	251	273	
Ge 76	14.3	70.3	9.0	36.2	
As 75	249	439	205	311	
Se 74	0.0	0.0	0.0	0.0	
Se 76	408	276	333	259	763.1
Se 77	269	224	218	202	
Se 78	345	380	270	299	
Se 80	133	157	95.8	110	
Se 82	3.7	29.7	1.7	12.5	
Br 79	228	273	174	203	
Br 81	128	89.5	91.1	71.7	
Kr 78	0.0	0.0	0.0	0.0	
Kr 80	123	33.0	106	46.9	675.5
Kr 82	251	218	169	164	495.9
Kr 83	109	124	71.0	84.1	
Kr 84	66.1	82.4	51.1	58.0	
Kr 86	103	114	73.0	78.0	224.3
Rb 85	100	121	87.8	87.5	
Rb 87	171	236	134	180	292.3
Sr 84	0.0	0.0	0.0	0.0	
Sr 86	100	99.5	103	114	147.4
Sr 87	28.9	44.3	46.8	57.3	57.3
Sr 88	33.2	35.1	39.8	41.2	
Y 89	32.5	34.9	35.1	37.4	
Zr 90	13.0	13.5	12.5	13.1	
Zr 91	19.6	20.0	20.9	21.7	
Zr 92	18.2	17.1	18.1	17.8	
Zr 94	13.7	14.9	11.4	12.5	
Zr 96	38.8	44.0	20.9	23.8	
Nb 93	27.1	27.9	25.2	26.5	
Mo 92	0.0	0.0	0.0	0.0	
Mo 94	0.0	0.0	0.0	0.0	
Mo 95	45.2	46.7	33.3	33.9	
Mo 96	8.7	7.1	6.3	6.5	
Mo 97	5.1	6.8	3.2	5.2	
Mo 98	3.4	6.2	2.2	3.8	
Mo 100	0.0	1.5	0.0	0.6	

Note. The corresponding results obtained with ^{22}Ne + α rates of Angulo et al. 1999 (Model 2) and of Raiteri et al. 1991a (Ra91b) are reported for comparison.

^{22}Ne + α rates lead to a higher ^{22}Ne consumption in the He core, leaving less for the C-burning phase. This also implies that the *s* yields are in general higher in Model 2. Despite these differences, the *s*-process nucleosynthesis described by the two models is rather similar. For this reason we focus our analysis on Model 1, and similar conclusions may be derived for Model 2.

As can be seen in Table 8, the final neutron burst in Model 1 causes an increase of the neutron exposure by 10% at $T_9 = 1.4$, from 0.087 mbarn^{-1} to 0.096 mbarn^{-1}. The ^{22}Ne available at C ignition is mostly consumed by the first neutron peak in the constant temperature phase, but a small amount is left (less than 10% with respect to the ^{22}Ne left behind in the He core ashes), boosting the neutron density and the n_c parameter. A local neutron capture process is activated feeding neutron-rich isotopes involved in branching points on the *s*-process path.

The amount of ^{22}Ne consumed in the C shell is comparable with the ^{22}Ne consumed in the He core. However, the burning conditions and the isotopic abundances are different in the two cases. For instance, in the C shell the light primary isotopes (among them ^{20}Ne, ^{23}Na, and ^{16}O) and the secondary isotopes (e.g., ^{25}Mg) capture more than 90% of the neutrons in the C shell, whereas this fraction is less than 80% in the He core.

The evolution of the neutron density and of the n_c parameter is plotted in panel (a) of Figure 3, as a function of the neutron exposure. The neutron density shows an initial peak, followed by a rapid decrease due to the ^{22}Ne depletion (neutron freeze-out) and by the final neutron burst, due to the temperature increase. As mentioned before, n_c strongly increases during this final neutron burst, whereas τ is marginally affected.

In panel (b), we report the abundance evolution of the Fe, Co, and Ni isotopes. To help the reader in the following analysis, Figure 4 illustrates the *s*-process path at neutron densities typical of the C shell in comparison with the classical low neutron density *s*-process path of the He core.

^{56}Fe is depleted by more than a factor of 2 in the C shell. ^{57}Fe shows a peak of production and then starts to decrease, following the depletion of ^{56}Fe. ^{58}Fe, the most abundant iron isotope after core He-burning, is partially consumed by the *s*-process in the C shell. During the first neutron density peak ^{59}Co rapidly decreases. The reason is that the ^{59}Fe branching between β^--decay and neutron capture is open, producing a significant amount of ^{60}Fe (e.g., Arnett & Wefel 1978; Chieffi & Limongi 2002, and references therein). In the neutron freeze-out, ^{59}Co is produced again and is slightly depleted in the final neutron burst. ^{60}Ni follows the ^{59}Co behavior due to the ^{59}Fe branching, and to the accumulation of ^{60}Fe. Indeed, ^{60}Ni is only produced by β^--decay of ^{59}Fe and subsequent neutron capture on ^{59}Co. ^{61}Ni shows a peak and then slightly decreases, as in the case of ^{57}Fe. The production of ^{62}Ni is in equilibrium with its depletion channel via neutron capture. ^{64}Ni increases during the entire C shell phase, in particular in the first part because the neutron capture channel in the ^{63}Ni branching is favored with respect to the β^--decay to ^{63}Cu.

Figures 5–7 provide an overview of the abundance changes during the shell C-burning phase for progressively higher mass intervals beyond Ni. In panel (a) of Figure 5, one finds that ^{63}Ni ($t_{1/2} \sim 0.4$ yr at 90 keV) behaves as a stable isotope and is accumulated according to its neutron capture cross section. During neutron freeze-out, ^{63}Ni starts to decay to ^{63}Cu, until the neutron density increases in the final burst. The ^{63}Cu previously produced in the He core is depleted by neutron capture, and the final ^{63}Cu in the C shell material is mostly produced via radiogenic decay of ^{63}Ni. The ^{65}Cu abundance is weakly affected by the C shell nucleosynthesis. Its initial increase due to ^{63}Cu depletion is followed by a small decrease, where its abundance is fed by neutron capture on ^{64}Ni.

^{64}Zn is produced only via the *s* path ^{62}Ni(n,γ)^{63}Ni($\beta^-\nu$)^{63}Cu(n,γ)^{64}Cu($\beta^-\nu$)^{64}Zn. Since ^{63}Ni has a long half life, the ^{64}Zn produced in the He core is depleted by neutron capture, and during freeze-out the neutron exposure is not high enough to produce again a significant amount of ^{64}Zn.

The abundances of ^{66,67,68,70}Zn and ^{69,71}Ga are plotted in panel (b) of Figure 5. At $n_n \sim 8 \times 10^{10}$ cm^{-3}, the abundance of ^{66,67}Zn reach a peak and then slowly decrease. Both isotopes are not affected by any branching. The ^{68}Zn abundance increases

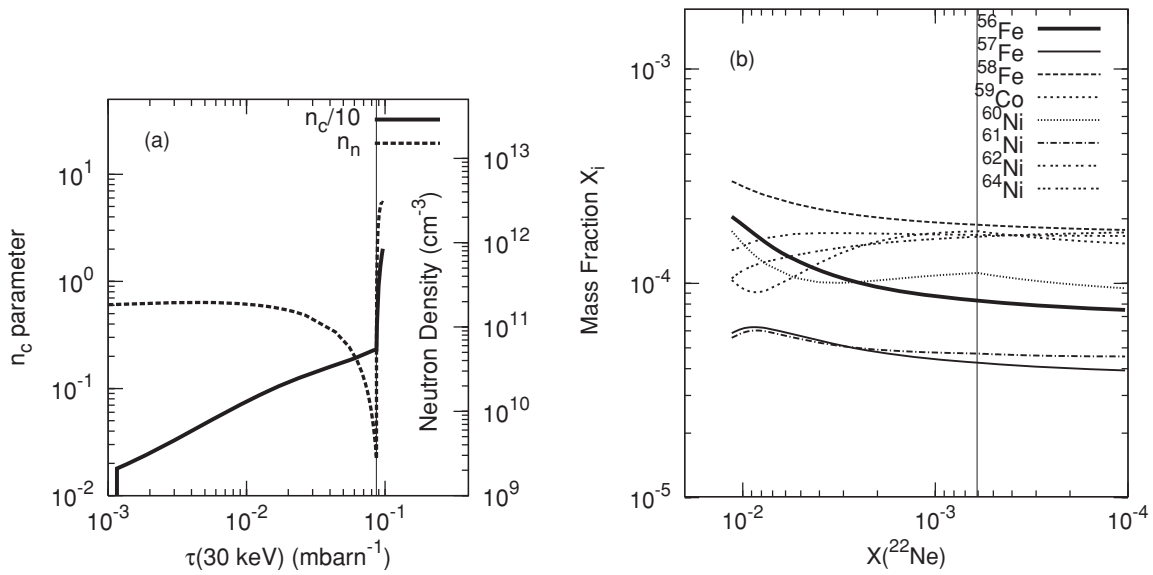

Figure 3. (a) Evolution of the n_c parameter and of the neutron density vs. neutron exposure (given at 30 keV) during convective C-burning shell. The vertical line at $\tau = 0.087$ mbarn^{-1} indicates when the temperature starts to increase in the shell. (b) Evolution of the mass fractions of ^{56,57,58}Fe, ^{59}Co, and ^{60,61,62,64}Ni during convective shell C shell burning. The vertical line at $X(^{22}\text{Ne}) = 6.07\times10^{-4}$ indicates when the temperature starts to increase in the shell.

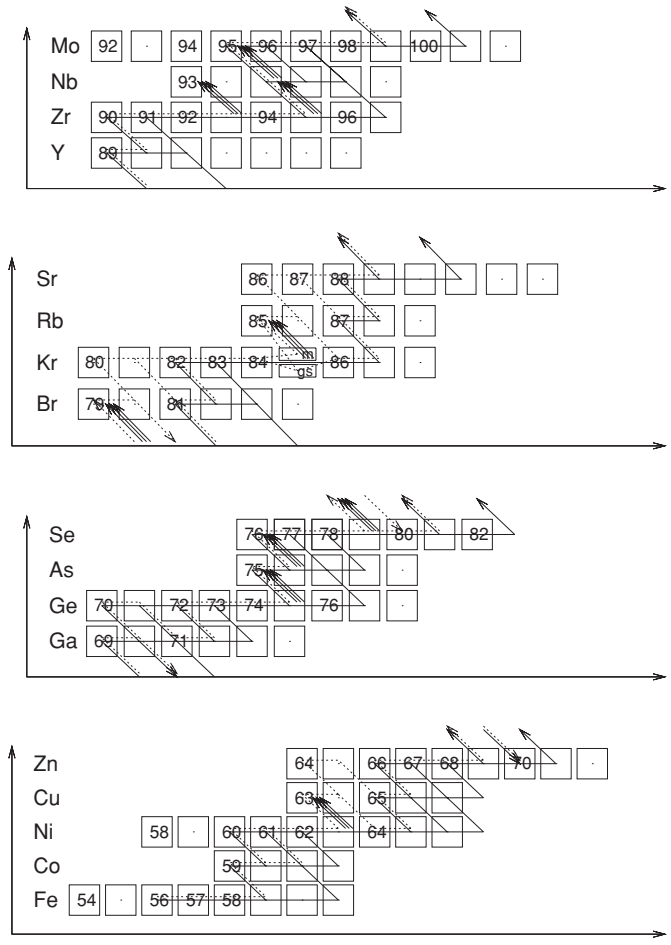

Figure 4. *s* path at neutron densities typical of the C shell (solid line) is shown in comparison with the *s* path in the He core (dotted line). Stable isotopes are indicated with their mass number. Triple-arrows indicate relevant radiogenic decay contribution after C shell nucleosynthesis.

with neutron exposure and remains almost constant during freeze-out and in the final burst. The *r*-only nucleus ^{70}Zn is produced when the ^{69}Zn branching is open during the initial high neutron-density phase and during the final neutron burst. This behavior is similar to ^{76}Ge and ^{82}Se (Figure 6), which are otherwise predominantly produced by the *r*-process. Their production depends critically on the occurrence of the final neutron burst, since they can be rapidly fed by local neutron capture fluxes starting from ^{68}Zn, ^{74}Ge, and ^{80}Se, respectively. The final neutron density is strongly affected by the amount of ^{22}Ne left in the C shell.

The ^{69}Ga abundance is increased by ^{68}Zn(n,γ)^{69}Zn($\beta^-\nu$)^{69}Ga. However, if the final neutron burst occurs, ^{69}Ga is slightly depleted because of the re-activation of the ^{69}Zn branching. ^{71}Ga strongly decreases in the first neutron peak, since the ^{71}Ge(n,γ)^{72}Ge channel is favored with respect the decay channel ^{71}Ge($\beta^+\nu$)^{71}Ga. With the decreasing of the neutron density, however, ^{71}Ga rapidly increases again.

Panel (a) in Figure 6 shows the situation for ^{70,72,73,74,76}Ge and ^{75}As. The abundance of the *s*-only isotope ^{70}Ge reaches an equilibrium value between production and destruction. It partially decreases in the final neutron burst, due to the activation of the ^{69}Zn branching for neutron densities larger than 10^{12} cm^{-3}. Note that the 10% *p*-process contribution to the solar ^{70}Ge (Käppeler et al. 1989) is not considered in the plot. The abundance behavior of ^{73,74}Ge is not affected by branchings. The final amount of ^{75}As produced in the C shell depends on the activation of the ^{75}Ge branching. At high neutron densities, in particular during the last neutron burst, neutron capture on the abundant ^{74}Ge feeds the production of the unstable ^{75}Ge, which is accumulated, and of the *r*-only ^{76}Ge. Once the neutron flow is exhausted, the residual amount of ^{75}Ge decays to ^{75}As.

Among the isotopes in panel (b) ^{76}Se is an *s*-only, but as in case of ^{70}Ge about 10% of solar ^{76}Se is contributed by the *p*-process (Käppeler et al. 1989). The partial activation of the branching at ^{76}As affects the final ^{76}Se yield in the C shell. Also the ^{77}Se yields are influenced by the activation of a branching at ^{77}As in the final neutron burst, for neutron densities of approximately 10^{12} cm^{-3}. ^{80}Se is produced during the entire C shell phase, since the neutron capture channel at the ^{79}Se branching is always open.

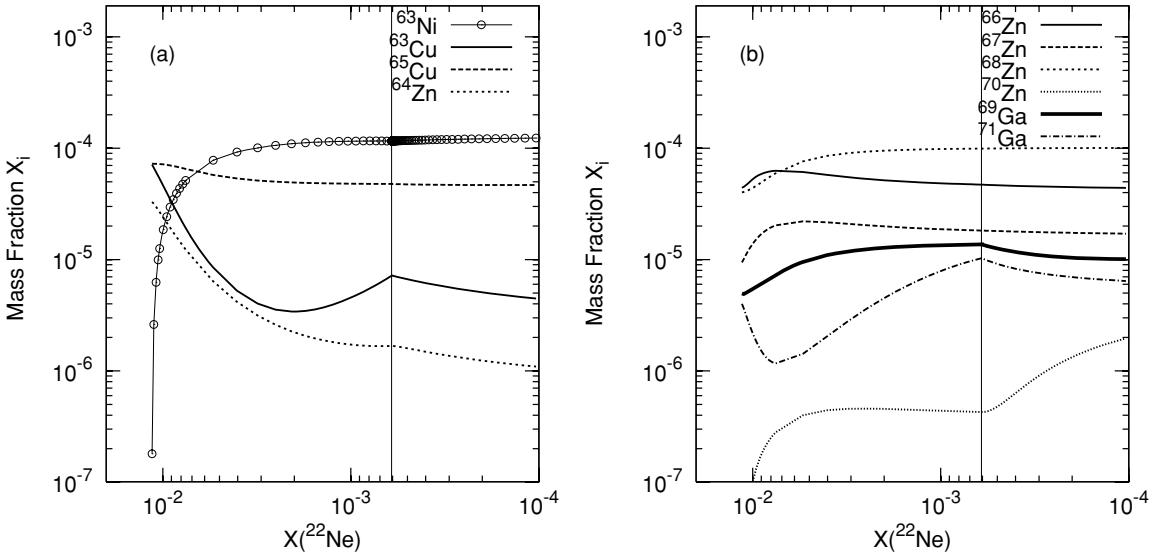

Figure 5. Evolution of heavy isotopes during convective C-burning shell. The vertical line at $X(^{22}\mathrm{Ne}) = 6.07\times10^{-4}$ indicates when the temperature starts to increase in the shell.

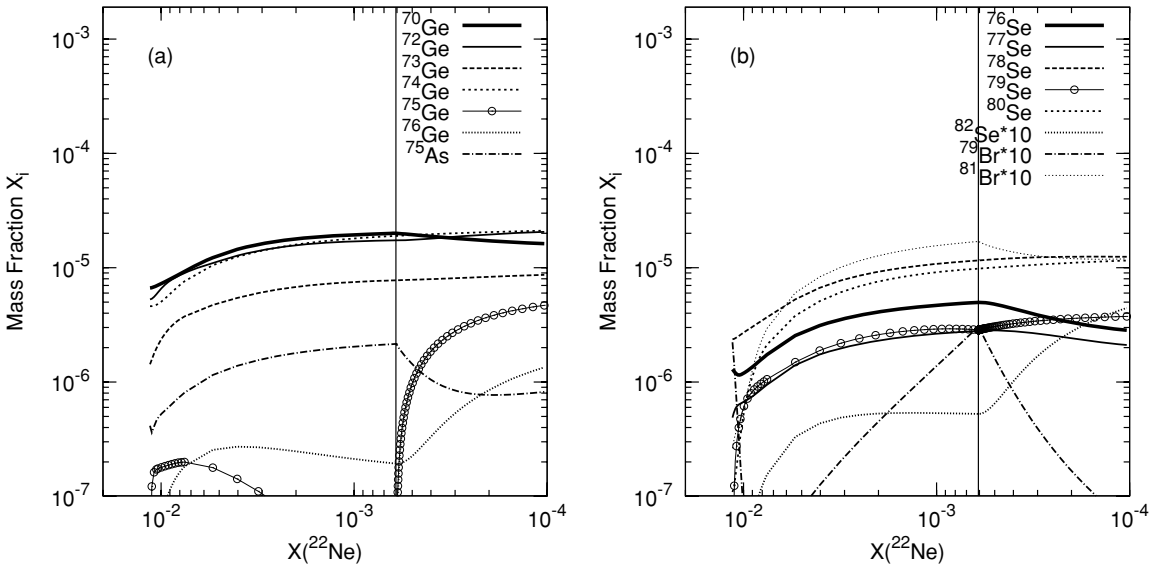

Figure 6. Evolution of heavy isotopes during convective C-burning shell. The vertical line at $X(^{22}\mathrm{Ne}) = 6.07\times10^{-4}$ indicates when the temperature starts to increase in the shell.

Because of the ^{79}Se branching, the ^{79}Br abundance decreases during both the first and the second neutron density peak, and is produced during the neutron freeze-out. In the C shell, a significant amount of the final ^{79}Br is made by the radiogenic decay of ^{79}Se. ^{81}Br is produced via ^{79}Br(n,γ)^{80}Br(n,γ)^{81}Br and via ^{80}Se(n,γ)^{81}Se($\beta^-\nu$)^{81}Br. At neutron densities typical of the first peak, neutron capture on the unstable ^{80}Br is efficient. The depletion of ^{81}Br during the second neutron burst is due to the activation of ^{81}Se branching, and part of the final *s* abundance of ^{81}Br is produced as ^{81}Se.

The Kr isotopes shown in panel (a) of Figure 7 are important because they include the two *s*-only nuclei ^{80,82}Kr and the neutron magic nucleus ^{86}Kr. The ^{80}Kr production (in this case 15% of the its solar abundance is made by the *p*-process, Käppeler et al. 1989) is affected by the ^{79}Se branching and by the related nuclear uncertainties. In the initial neutron density regime of the C shell, the ^{80}Kr produced in the previous He core is rapidly depleted. During neutron freeze-out it starts to be rebuilt, and in the final neutron burst it is depleted again. The occurrence of a second neutron density peak and its strength define the final ^{80}Kr in the C shell (see Section 7 for a more detailed discussion about the *s* nucleosynthesis of ^{80}Kr). The *s*-only ^{82}Kr shows a decrease before increasing again during the neutron density freeze-out. The ^{83}Kr production at C shell ignition is fed by the neutron capture path ^{80}Kr(n,γ)^{81}Kr(n,γ)^{82}Kr(n,γ)^{83}Kr, and for this reason a small initial abundance peak is observed, ending because of the ^{80}Kr depletion. ^{84}Kr is not affected by branchings and increases during the entire neutron exposure. The neutron magic nucleus ^{86}Kr is efficiently produced in the C shell, since the ^{85}Kr branching is open and because of its low neutron capture cross section (MACS (30 keV) = 4.54 mbarn; Mutti et al. 2005).

Finally, ^{85}Kr, ^{85,86,87}Rb, and ^{86,87,88}Sr are plotted in panel (b). When $n_\mathrm{n} \gtrsim 10^{11}$ cm^{-3}, the unstable isotope ^{85}Kr is accumulated

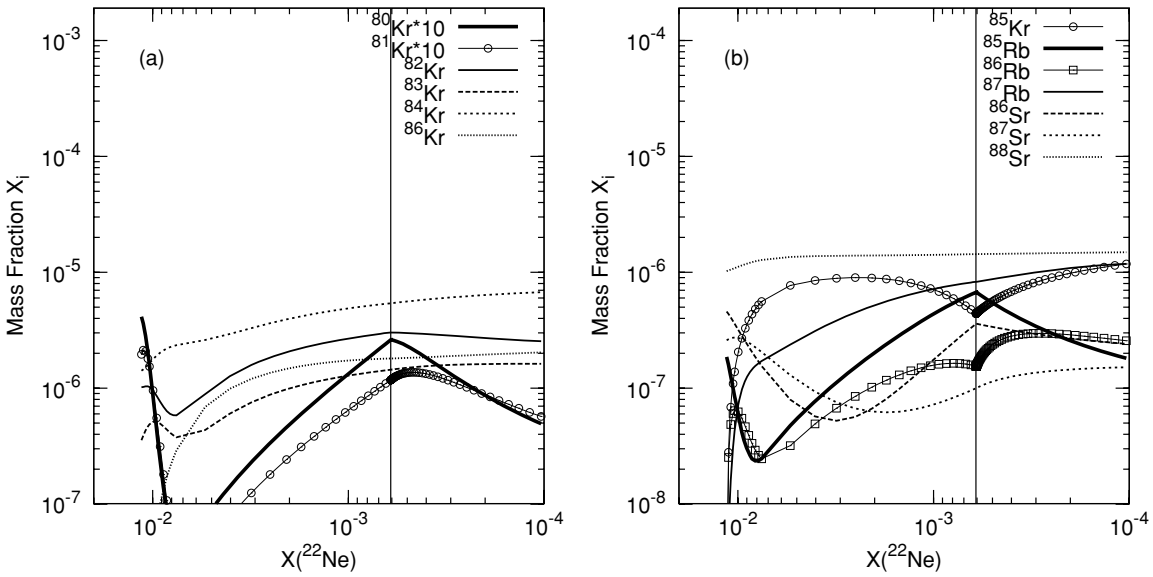

Figure 7. Evolution of heavy isotopes during convective C-burning shell. The vertical line at $X(^{22}\mathrm{Ne}) = 6.07\times10^{-4}$ indicates when the temperature starts to increase in the shell.

and ^{85}Rb is depleted. During the neutron freeze-out only a fraction of ^{85}Kr decays to ^{85}Rb, and in our calculations most of ^{85}Rb is of radiogenic origin. The neutron magic nucleus ^{87}Rb is continuously accumulated, in particular via the production channel ^{85}Rb(n,γ)^{86}Rb(n,γ)^{87}Rb, first fed by the abundant ^{85}Rb produced in the previous He core, and then by the ^{85}Rb built during the neutron freeze-out via the ^{85}Kr decay. The final *s*-process abundance of ^{87}Rb is mainly produced in shell C-burning (see also The et al. 2007), increasing with neutron exposure and with the ^{22}Ne abundance left in the ashes of the He core. The ^{86}Rb $t_{1/2}$ is $\sim$ 20 days at C-burning temperatures. Its abundance is directly affected by the evolution of ^{85}Rb, and it accumulates in the high neutron density regimes of shell C-burning.

The production of the *s*-only ^{86,87}Sr (5.6% of the ^{86}Sr solar abundance and 3% of ^{87}Sr are made by the *p*-process, Käppeler et al. 1989) is determined by the ^{85}Kr branching. Panel (b) shows that ^{86}Sr receives a significant radiogenic contribution from ^{86}Rb for neutron densities in excess of 10^{12} cm^{-3}. At the end of the neutron burst, the amount of ^{86}Rb is comparable with that of ^{86}Sr. Therefore, the final abundance ratio ^{86}Sr/^{87}Sr is affected by the uncertainty of the neutron capture rate of ^{86}Rb.

The *s*-process yields of the yttrium, zirconium, niobium, and molybdenum isotopes are included in Table 9. Beyond the Sr–Y–Zr peak, a significant contribution is still observed for ^{93}Nb and ^{95}Mo, both being produced via radiogenic decay of ^{93}Zr and ^{95}Zr, respectively.

The final *s* yields in the C shell (Model 1, Table 9) are plotted in Figure 8 normalized to the abundances before the C shell temperature starts to increase (see Table 9, Column 2). As already mentioned before, the *s* distribution is not generally affected by the final neutron burst. We obtain some additional production of ^{70}Zn, ^{76}Ge, ^{82}Se, and ^{100}Mo. On the other hand, the abundance of ^{80}Kr and of the *p*-only ^{94}Mo decreases. The production factor of ^{75}As and, the ^{70}Ge/^{70}Zn and the ^{76}Se/^{76}Ge ratios are indicators of the final peak neutron density. Concerning ^{75}As, we refer to the next section for further discussion. The isotopic ratio ^{70}Ge/^{70}Zn changes from 15.0 to 3.1 in Model 1 (19.3 to 4.7 in Model 2), and ^{76}Se/^{76}Ge from 28.5 to 3.9 (36.8 to 7.1 in Model 2).

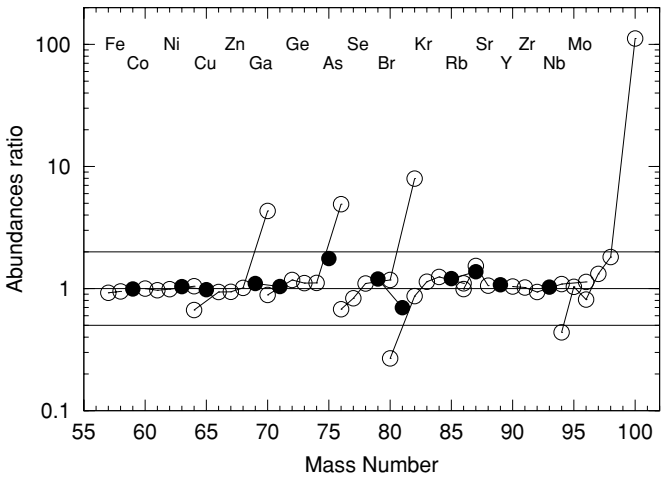

Figure 8. Abundance ratio of the isotope distribution between ^{57}Fe and ^{100}Mo at the end of convective C shell burning ($T_9 = 1.40$) with respect to the distribution before the temperature starts to increase in the shell ($T_9 = 1.05$). Radiogenic contribution from the decay of unstable isotopes is considered. Isotopes of the same elements are connected with a line. Elements with even and odd *Z* are distinguished by black and open symbols. Two lines indicating a variation by a factor of 2 are included.

5. EFFECT OF NUCLEAR UNCERTAINTIES

In massive stars the final *s*-process yields are strongly affected by the uncertainty of the ^{22}Ne + α capture rates during core He-burning ($kT \sim 30$ keV), both by the total α-capture rate and by the (α,n)/(α,γ) reaction rate ratio. We refer to previous works (e.g., Rauscher et al. 2002, and reference therein) and to the previous sections, where we presented *s*-process distributions calculated using different ^{22}Ne + α rates (Sections 3 and 4). During shell C-burning ($kT \sim 90$ keV) the ^{22}Ne depletion is dominated by the ^{22}Ne(p,γ)^{23}Na and by the ^{22}Ne(α,n)^{25}Mg reactions, whereas the ^{22}Ne(α,γ)^{26}Mg channel is marginal, as shown in Figure 9. At C-burning temperatures, the uncertainty of the ^{22}Ne(α,n)^{25}Mg rate is significantly lower than at He-burning temperatures. On the other hand, the uncertainty of the two dominating C-burning channels ^{12}C(^{12}C,α)^{20}Ne and

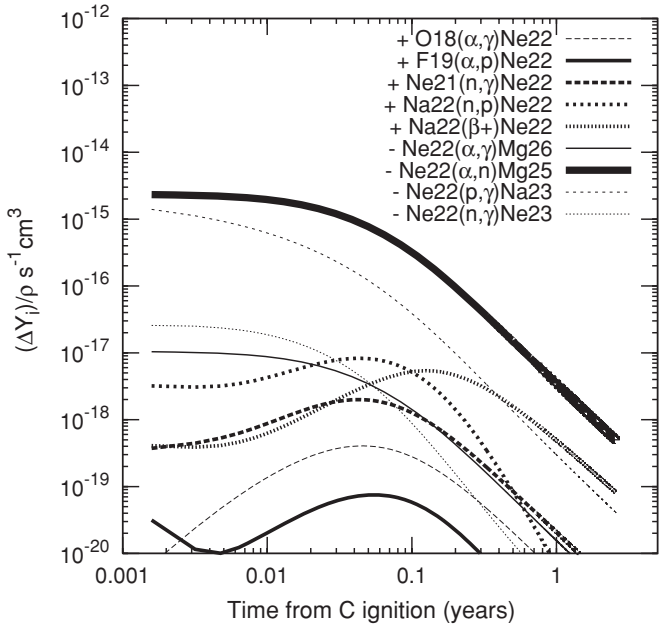

Figure 9. Production and destruction nucleosynthesis channels of ^{22}Ne vs. evolution time in C shell burning. For simplicity, the C shell temperature is kept constant ($T_9 = 1.05$) until ^{22}Ne depletion.

^{12}C(^{12}C,p)^{23}Na may affect the amount of neutrons produced by ^{22}Ne.

Furthermore, other charged particle reactions may affect the *s*-process calculations, including the nuclear reactions providing energy for stellar evolution. For instance, we mention the triple-α reaction (Tur et al. 2009) and the ^{12}C(α,γ)^{16}O during He-burning (in competition with the ^{22}Ne(α,n)^{25}Mg; e.g., Raiteri et al. 1991b; Käppeler et al. 1994; Imbriani et al. 2001; Woosley & Heger 2007; Tur et al. 2009; El Eid et al. 2009), and the ^{12}C + ^{12}C during C-burning (M. Pignatari et al. 2010, in preparation). ^{12}C(α,γ)^{16}O affects the amount of ^{12}C left in the ashes of the He core, and the ^{12}C + ^{12}C rate is providing α particles and protons to burn ^{22}Ne. Depletion of ^{22}Ne is efficient in shell C burning conditions, and it is reasonable to assume that in the C shell material the ^{22}Ne still available after the He core will be mostly destroyed before the SN explosion. On the other hand, the ^{12}C left and the ^{12}C + ^{12}C rate are affecting the C-burning ignition in the core, convectively or radiatively, and in the convective C shell, the C-burning temperature and density at the shell bottom and its evolution timescale. For these reasons, such reactions are affecting the neutron density history, whereas without considering drastic rate changes the neutron exposure is more affected by the amount of ^{22}Ne available.

In general, the variation of important charged particle reaction rates in the nuclear network affects *all* the heavy *s* isotopes by increasing (or reducing) the total neutron exposure and the neutron capture per iron seed. This scenario becomes more complicated if we consider the uncertainties in the neutron capture network.

After the compilation of Bao et al. (2000), an increasing number of measurements (e.g., Nassar et al. 2005; Heil et al. 2008b) provided new neutron capture cross sections of isotopes between Fe and Sr. They had a significant impact on the *s*-process in massive stars, showing that these nucleosynthesis calculations crucially depend on improvements in the nuclear network, in particular in the high temperature and high neutron density regime of shell C-burning. The MACS of most isotopes

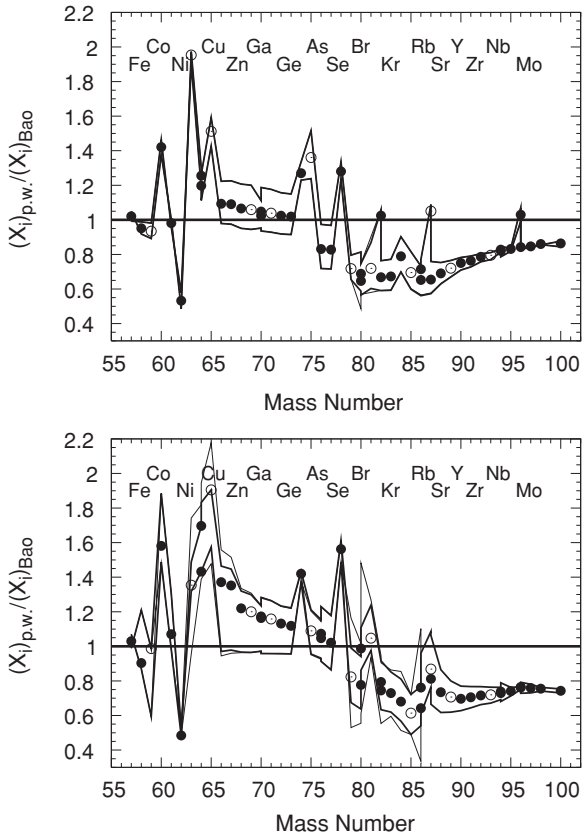

Figure 10. Top: nucleosynthesis yields between ^{57}Fe and ^{100}Mo at the end of the He core (present work) relative to the distribution obtained using the MACS beyond iron by Bao et al. (2000). The thick lines correspond to the maximum and minimum yields using the new recommended rates, and their upper and lower limits. The thin lines correspond to the maximum and minimum yields if a factor of 2 of uncertainty for the MACS of the unstable isotopes ^{63}Ni, ^{79}Se, and ^{85}Kr is included. Elements with even and odd *Z* are distinguished by black and open symbols. Bottom: the same comparison at the end of C shell burning.

between Fe and Sr are lower than $\sim$ 150 mbarn, thus acting as bottle−necks along the neutron capture flow. The variation of *one* of them causes a propagation effect over *all* the heavier *s* abundances, whereas previous isotopes in the *s* path are substantially unaffected. As a consequence, different *s*-process abundance distributions are obtained with the same neutron exposure and neutron capture per iron seed, but using different neutron capture networks. The uncertainty of the cross sections between Fe and Sr affects the final *s*-process yields in a way that is difficult to predict, compromising the possibility to provide reliable weak *s* component predictions. Most of the *s*-process-rich material ejected by a 25 $M_\odot$ star has been processed by both the He core (neutron exposure at $kT \sim 30$ keV) and the C shell (neutron exposure at $kT \sim 90$ keV). For this reason, all these bottleneck neutron capture cross sections should be determined with the highest possible experimental accuracy (10% or less) at 30 keV *and* at 90 keV.

The upper panel of Figure 10 presents the *s*-process distribution at the end of the He core obtained using the new MACS beyond iron normalized to the distribution obtained with the rates from Bao et al. (2000). The general behavior of the new distribution with respect to previous calculations is characterized by the superposition of the effect due to the new higher ^{62}Ni MACS by Alpizar-Vicente et al. (2008) with the impact of the new MACS for the iron group, in particular the lower values for ^{63,65}Cu by Heil et al. (2008b), which are responsible for a

propagation effect in the Zn–Ge region. Between ^{65}Cu and ^{73}Ge, the use of the new MACS increases the previous abundances obtained using Bao et al. (2000) by up to 25%.

For heavier isotopes, the new distribution is dominated by the propagation effect of the new ^{74}Ge MACS by Marganiec et al. (2009) and the ^{78}Se MACS by Dillmann et al. (2006), both lower than the previous rates of Bao et al. (2000). Therefore, the resulting *s*-process distribution between Br and the Sr–Y–Zr peak is generally lower as well. Figure 10 also includes the effect of an estimated uncertainty of a factor of 2 for the MACS of ^{63}Ni, ^{79}Se, and ^{85}Kr. These unstable isotopes give rise to branchings in the *s* path. In the He core, the only noticeable effect comes from ^{79}Se, but the situation is significantly more complicated at the end of shell C-burning (bottom panel of Figure 10). First, as shown by Heil et al. (2008b), the MACS uncertainties are higher at 90 keV than at 30 keV. For instance, the new ^{66,67}Zn yields could be more than 40% higher or 5% lower than the old yields obtained with the rates of Bao et al. (2000). Beyond ^{78}Se, the distribution is lower by a factor of 0.6–0.8. A few exceptions, e.g., ^{87}Br, and variations from the general trend are due to the impact of the new Br-Rb MACS by Heil et al. (2008a) and the new Kr MACS by Mutti et al. (2005). Second, the *s*-process branchings at ^{63}Ni, ^{79}Se, and ^{85}Kr are fully open. In this case, the MACS uncertainties of the unstable branching point nuclei are propagated locally to the subsequent stable isotopes and are affecting the final yields of copper, bromine, krypton, and strontium.

The *s*-process distributions in Figure 10 were obtained without taking the uncertainties of the large sample of MACS with old measurements, e.g., ^{66,67,68}Zn, ^{69,71}Ga, ^{72,73}Ge, ^{77}Se into account. For this reason, new MACS measurements can significantly improve further the reliability of *s*-process calculations, in particular in He-burning conditions.

The weak *s* predictions are also affected by the uncertainties of the neutron capture cross sections of the light neutron poisons. In this case, the choice of a different MACS is propagated over the entire abundance distribution. Usually, the production of elements close to the Sr peak is more affected than elements close to the iron seeds. For instance, ^{23}Na is an important neutron poison in the C shell. The use of a different MACS of ^{23}Na affects mostly of the weak *s* yields (for details see Heil et al. 2007). Other examples are the effect of the uncertainty of the ^{22}Ne MACS (Busso & Gallino 1985; Langer et al. 1989), or of the ^{16}O MACS, in particular at subsolar metallicities (Rayet & Hashimoto 2000). ^{16}O is the strongest neutron absorber during core He-burning and shell C-burning. The neutrons captured are mostly recycled via the ^{17}O(α,n)^{20}Ne reaction, but a large fraction of them is recaptured by ^{16}O again, depending on the low and uncertain MACS (Bao et al. 2000).

The conclusion that we derive from Figure 10 is that theoretical predictions for the weak *s* component are affected by large nuclear uncertainties regarding the neutron capture cross sections, uncertainties that need to be addressed.

In Figure 11, the elemental overabundances (El/El$_{sun}$) in the C shell material are shown for several cases compared with Model 1 (case 1). The error bars associated with this distribution include the effects of the neutron capture uncertainties discussed in the bottom part of Figure 10. The comparison between cases 1 and 2 confirms that the new sample of MACS used in this work causes an increase of the *s*-process efficiency up to Se. The decrease in efficiency beyond Se is due to the propagation effect of the new ^{74}Ge and ^{78}Se MACS. The comparison between case 1 and cases 3, 4 shows the effect of different

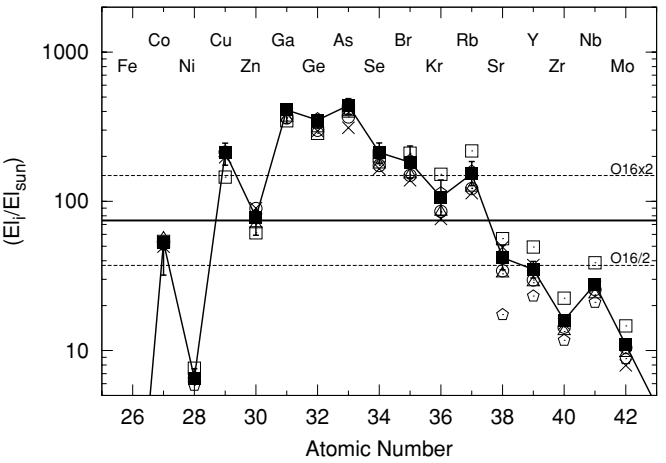

Figure 11. Element overabundances between Fe and Mo at the end of convective C shell burning. Case 1 corresponds to Model 1 at the end of C shell burning (black squares and solid line). Errorbars refer to MACS uncertainties discussed in Figure 10. For comparison, case 2 (open squares) corresponds also to Model 1 but was calculated using the MACS data of Bao et al. (2000). Case 3 (crosses) corresponds to Model 2, using the ^{22}Ne + α by Angulo et al. (1999), and case 4 (open triangles) was obtained with Model 1 using the lower limit of the ^{22}Ne(α,n)^{25}Mg rate by Jaeger et al. (2001). Case 5 was calculated as case 1 but reducing ^{66,67,68}Zn MACS by 20% with respect to Bao et al. (2000; open circles), and case 6 using terrestrial β-decay rates (open pentagons).

^{22}Ne + α rates, which starts to be evident beyond Zn, whereas the *s*-process yields in Fe–Co–Ni–Cu region are not strongly affected because isotopes close to iron seeds reach the final equilibrium abundances at lower neutron exposures. Therefore, the *s*-process predictions for these elements are more robust, even for the reduction of the ^{22}Ne(α,n)^{25}Mg rate by a factor of 2. Larger variations of the present recommended rate appear to be excluded in view of the experimental situation (e.g., Ugalde 2008), which supersedes for example the upper limit given in NACRE and as well the related interpretations (e.g., Costa et al. 2000). Any sensible enhancement of the ^{22}Ne(α,n)^{25}Mg rate would be in disagreement with the main *s* component (e.g., Busso et al. 2001) and with the precise measurements of presolar grains from AGB stars as well (e.g., Lugaro et al. 2003). The comparison between cases 1 and 5 shows the propagation effect of the ^{66,67,68}Zn MACS, which was not considered in Figure 10 since new measurements have not yet been published for these isotopes (M. Heil 2008, private communication). Preliminary indications point to a lower MACS than reported in Bao et al. (2000), at least for ^{68}Zn. Although a linear propagation effect is caused by the cross sections of ^{66,67,68}Zn in the He core and in the C shell, the present calculations show that the *s*-process contribution to zinc at the end of the C shell is smaller compared to neighbor elements. This is illustrated in Figure 11, where a 20% reduction was assumed for the MACS of the Zn isotopes. Case 6 shows the effect of using terrestrial β-decay rates, without considering temperature or density dependence in He-burning and C-burning conditions for such reactions (see Section 2 for the β-decay rates used, e.g., in Model 1). Indeed, the half life of a group of unstable isotopes are strongly dependent in stellar conditions (e.g., ^{79}Se, ^{81}Kr, ^{85}Kr at 90 keV, and ^{99}Mo), typically decreasing with increasing temperature. Concerning elemental abundances, in Figure 11 no significant variation from Model 1 is observed up to Kr. Then, the use of the terrestrial ^{85}Kr decay rate during C-burning ($t_{1/2}$ = 10.76 yr compared to $t_{1/2} \sim$ 0.1 yr at 90 keV) drastically underestimates the nucleosynthesis flow starting from ^{85}Kr(β^-)^{85}Rb, and feeding ^{87}Rb, all Sr isotopes

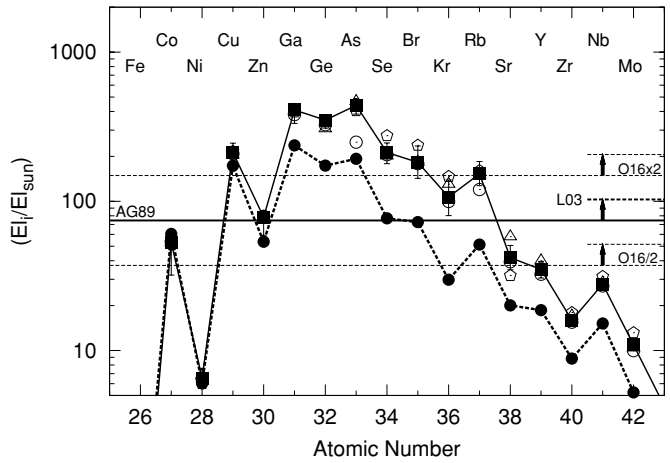

Figure 12. Element overabundances between Fe and Mo at the end of convective C shell burning of case 1 (black squares and solid line; see Figure 11) is compared with case 7, giving the distribution at the end of the constant temperature phase (open circles), with cases 8 and 9 where the efficient temperature during the constant temperature phase is T9 = 1.0 and T9 = 1.1, respectively (open pentagons and open triangles, respectively), and with case 10 (black circles and dashed line). Case 10 was obtained with Model 1, starting from initial abundances by Lodders (2003; according to prescriptions of Piersanti et al. 2007) instead of Anders & Grevesse (1989). The ^{16}O overproduction according to (Anders & Grevesse 1989; AG89 in the figure, solid line) is compared on the right with the new solar from (Lodders 2003; L03, dashed lines).

and beyond. ^{86}Kr is overproduced by about 40%. On the other hand, production of Sr, Y, Zr, Nb, and Mo decreases by a factor of 2.4, 1.5, 1.3, 1.3, and 1.2, respectively, compared to Model 1. The yields of ^{87}Rb decrease by a factor of 3.8, but Rb production is compensated by a higher production of ^{85}Rb via radiogenic decay of ^{85}Kr (see also Section 4).

Between cases 6 and *1* the total amount of Kr that is produced does not significantly change. However, in case 6 the terrestrial ^{79}Se decay rate ($t_{1/2} = 4.8 \times 10^5$ yr compared to $t_{1/2} \sim 0.4$ yr at 90 keV) closes the *s*-process path producing ^{80}Kr, which results to be destroyed at the end of the C shell. No important variations are observed for Br isotopes (below 5%), since ^{79}Br is mainly produced via radiogenic decay of ^{79}Se and ^{81}Br via ^{81}Se(β^-)^{81}Br (see also Section 4), and for ^{82}Kr (underproduced by about 10%).

Finally, Cu is not affected by using the ^{63}Ni terrestrial decay rate ($t_{1/2} = 100$ yr compared to $t_{1/2} \sim 2$ yr at 90 keV). Indeed, in both cases 1 and 6 the neutron capture channel at the ^{63}Ni branching is favored compared to the β-decay channel.

In Figure 12, uncertainties due to stellar model approximations and different choices of solar composition are considered. The comparison between cases 1 and 7 shows that a final temperature increase in the C shell has a significant effect only for the total production of As and Rb. Cases 8 and 9 show the effect of varying the burning temperature in our C shell simulations during the constant temperature phase (increasing and decreasing the burning temperature $T9 = 1.05$ by 5%, respectively). The same prescriptions of the standard case are used during the final temperature increase, that starts when 2/3 of initial carbon is left, according to Arnett & Wefel (1978). Its impact is well within the nuclear uncertainties between Fe and As, for Rb and beyond Y ($\lesssim$ 15%), excluding Mo. For Se, Br, Kr, Sr, and Mo the element production changes more significantly, with a maximum variation for Sr (by about 80%). For most of the elements included in this last group there is no clear relation between production efficiency and burning temperature. Exceptions are Sr and Mo, where Sr is more produced in case 8 (a lower temperature and a lower neutron density during the constant temperature phase opens the β^-decay channel in the ^{85}Kr branching favoring Sr production) and Mo is more produced in case 9 (a higher temperature and a higher neutron density builds up more ^{95}Zr, that will feed ^{95}Mo via radiogenic decay).

Finally, case 10 shows the *s*-process distribution obtained using the initial solar abundance by Lodders (2003), re-evaluated according to the analysis of Piersanti et al. (2007), whereas the solar distribution is given by Anders & Grevesse (1989) in all the previous cases. As also mentioned by Woosley & Heger (2007) and Tur et al. (2009), new solar abundances reported by Lodders (2003; but see also Asplund et al. 2005, 2009; Lodders et al. 2009) reduced solar CNO with respect to older compilations. This is directly affecting the weak *s*-process, since initial CNO is fully converted to ^{22}Ne, that produces neutrons starting from the He-burning core. Compared to Anders & Grevesse (1989), smaller variations in the solar isotopic abundances are also present due to new meteoritic analysis: ^{31}P goes down by 25%, ^{36}S and Cl are discussed in detail in Section 7.1 and we refer to that section, Se goes up by 5%–10%, Br down by about 5%, Rb down by about 5%, Nb up by 8%, Kr up by 20%–15% depending on the isotope, and Mo up by 10% (see Palme & Beer 1993). For a detailed discussion see Piersanti et al. (2007).

In Figure 12, we observe that in the Fe–Cu region the effect of the choice of the new CNO by Lodders (2003) is lower or comparable to nuclear uncertainties. Beyond Zn, the use of a different initial solar abundances set makes a larger variation in the *s* yields than nuclear or stellar model uncertainties considered in the previous discussion. Using the new CNO, copper overabundance decreases by about 20%, whereas Ge, Kr, and Sr decrease by a factor of 2.0, 3.6, and 2.1, respectively. For the *s*-process analysis in massive stars is crucial to define solar CNO abundances with high precision.

Summing up, the elements with a large *s* component at the end of the C shell of a 25 $M_\odot$ star with [Fe/H] = 0 are Cu, Ga, Ge, and As, that in all the cases considered are always overabundant with respect to ^{16}O. In case the initial solar composition by Anders & Grevesse (1989) is used like in Model 1, Model 2 and in all the other cases considered in Figures 11 and 12, we may add to the previous list also Se, Br, Kr, and Rb.

Beyond Sr the efficiency of the weak *s*-process decreases rapidly. In this mass region, the *s* abundances are mostly produced by the main *s* component in AGB stars (e.g., Travaglio et al. 2004a). Using Anders & Grevesse (1989) as initial composition, the peak of *s*-process abundances in Figures 11 and 12 is overproduced with respect to the line ^{16}O×2, in agreement with Rauscher et al. (2002) for a 25 $M_\odot$ star. In the case where Lodders (2003) composition is used, the most produced elements Cu, Ga, Ge, and As lie on such a line. For this reason, one could argue that using more recent solar abundances *s*-process yields of the 25 $M_\odot$ star better reproduce the solar system distribution.

We recall that the present results cannot be used to estimate the weak *s* component in the solar system, since they refer to only one stellar model. Indeed, also the contribution from lower and higher masses must be included, integrating the different stellar yields according to the initial mass function (IMF; e.g., Raiteri et al. 1993; The et al. 2007; Tur et al. 2009), and no conclusions concerning the weak *s* component can be derived so far. The purpose of this paper is to analyze the impact of the nuclear uncertainties on the weak *s*-process, showing that improvements for neutron capture cross

sections are required in order to obtain reliable *s*-process predictions.

Summing up, in this section: (1) we analyzed the impact of a new sample of MACS on the weak *s*-process at the end of the He-burning core and in the C shell; (2) the use of new MACS shows also a clear propagation effect over heavier *s* isotopes, up to the Sr peak; (3) MACS uncertainties are stronger at C shell temperatures, affecting the reliability of *s*-process predictions; (4) MACS of unstable isotopes has a local propagation effect in the C shell for several branching points, e.g., ^{63}Ni, ^{79}Se, and ^{85}Kr. In the He core these are relevant only for ^{79}Se; (5) MACS uncertainties of light neutron poisons are also propagated to the *s*-process distribution; (6) we studied the impact of the final neutron burst on the *s*-process yields. Only the elemental abundances of As and Rb are significantly affected; (7) production of Se, Br, Kr, Sr, and Mo are modified by changing by 5% the burning temperature in the initial constant temperature regime of the one-zone C shell model. In particular, Sr abundance increases with reducing burning temperature. The *s*-process yields of other elements between Fe and the Sr peak do not significantly change. (8) We provide a test where the initial distribution is given by Lodders (2003), compared to the other calculations using Anders & Grevesse (1989). We showed that beyond Zn weak *s*-process predictions are strongly affected by recent updates in the solar composition, in particular in the CNO abundances (see also Tur et al. 2009).

Finally, within a full set of nuclear and model uncertainties, we defined which elements are significantly produced by the weak *s*-process in our calculations. In particular, we showed that *s* isotopes in the Fe–Cu region are less affected by uncertainties in the nuclear network, in stellar models and by the update of the initial composition.

6. COMPARISON WITH OBSERVATIONS

As we mentioned in Section 5, the *s*-process yields of one star cannot be used to reproduce the weak *s* component. We need to include the contribution of a full generation of stars. In the same way, GCE calculations including *s* yields from a complete grid of stars are required to provide a detailed comparison with spectroscopic observations of elements in stars at different metallicities (e.g., Timmes et al. 1995).

In this section, we discuss recent observations which can provide important constraints for the weak *s*-process. Copper, gallium, and germanium are ideal elements to observe for testing *s*-process predictions for massive stars, since they are located at the peak of the *s*-process distribution (Figure 12; e.g., Rauscher et al. 2002; Chieffi & Limongi 2006; The et al. 2007). Heavier elements are either not observed (e.g., As), or receive important contributions from other nucleosynthesis processes. For example, Sr, Y, and Zr are also significantly produced by the *s*-process in AGB stars, by the *r*-process and by the LEPP (Travaglio et al. 2004a; Pignatari et al. 2008; Kratz et al. 2008; Qian & Wasserburg 2008; Farouqi et al. 2009). On the other hand, copper, zinc, gallium, and germanium are not efficiently produced by the *s*-process in AGB stars and, as pointed out by Kratz et al. (2008), spectroscopic observations of low metallicity stars confirm that they are also not produced by the main *r*-process.

6.1. Copper

Extensive spectroscopic analysis of copper started with Sneden & Crocker (1988) and Sneden et al. (1991) for stars

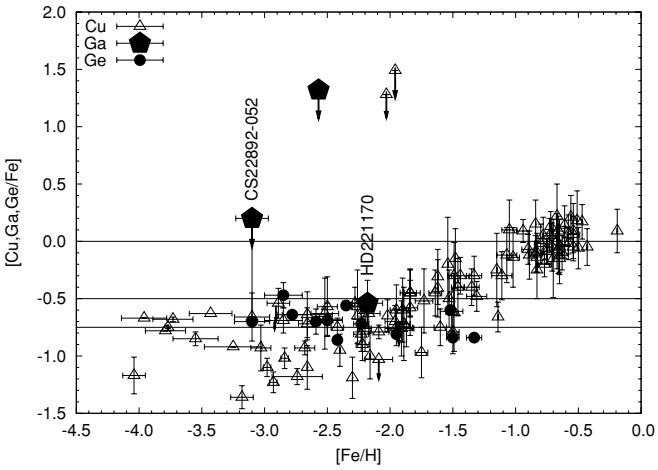

Figure 13. Spectroscopic observations of [Cu/Fe], [Ga/Fe] and [Ge/Fe] vs. [Fe/H] at low metallicity included in SAGA websource (Suda et al. 2008) as a compilation from different references. Copper observations (Lai et al. 2008; Cowan et al. 2002; Bihain et al. 2004; Mishenina et al. 2002; Ivans et al. 2003; Cohen et al. 2008; Sneden et al. 2003; Masseron et al. 2006; Johnson & Bolte 2004; Westin et al. 2000; Honda et al. 2004; Jonsell et al. 2006) are indicated with empty triangles, gallium (Sneden et al. 2003; Ivans et al. 2005, 2006) with full pentagons and germanium (Sneden et al. 1998; Cowan et al. 2005) with full circles. For the star CS22892 − 052 ([Fe/H] = −3.1), the observed upper limit for Ga is connected by a line with the Cu observed abundance (Sneden et al. 2003). Germanium and copper have similar abundances ($\lesssim$0.2 dex of difference). Finally, for the star HD221170 ([Fe/H] = −2.18) the abundances of copper, germanium, and gallium are all observed, with a good agreement between the three values.

at different metallicities in the Galaxy, showing a decreasing trend of [Cu/Fe] with decreasing metallicity, the typical behavior of a secondary element (e.g., Timmes et al. 1995; Woosley & Weaver 1995). In Figure 13, we report a sample of observations at metallicity lower than solar (Suda et al. 2008). For a larger collection of copper observations we refer to Bisterzo et al. (2005). The decreasing trend of [Cu/Fe] is observed in the metallicity range $-1.5 \lesssim$ [Fe/H] $\lesssim -0.5$. Sneden et al. (1991) proposed the *s*-process in massive stars as the main source for the solar copper. In disagreement with this scenario, Raiteri et al. (1991b) and Matteucci et al. (1993) showed that the weak *s*-process was only reproducing a minor part of the solar copper, suggesting a strong contribution (more than 50%) from supernovae Type Ia (SNe Ia). However, nucleosynthesis models of SNe Ia only reproduce a few percent of the solar copper (Hoeflich et al. 1998; Iwamoto et al. 1999; Travaglio et al. 2004b, 2005).

Recently, a new analysis of the large sample of copper observations available today at different metallicities (e.g., Bisterzo et al. 2005) re-proposed that most of the copper in the Galaxy is produced by the *s*-process in massive stars. This conclusion was also confirmed by GCE calculations from Romano & Matteucci (2007), based on massive star yields by Tominaga et al. (2007).

GCE simulations by Travaglio et al. (2004a) for the *s*-process contribution of AGB stars reproduce only $\sim$ 5% of the solar copper. Massive stars models confirm some primary explosive production of copper (e.g., Woosley & Weaver 1995), but the uncertainty in the position of the mass cut strongly affects theoretical predictions. An important constraint to quantify the primary copper component from massive stars is provided by spectroscopic observations below [Fe/H] ~ -1.5, where [Cu/Fe] shows a flat trend at $\lesssim -0.5$ (see Figure 13). If one adopts [Cu/Fe] $= -0.5$, the primary component of the solar copper is 11%–16% (assuming that 1/3 or 1/2 of the solar iron is

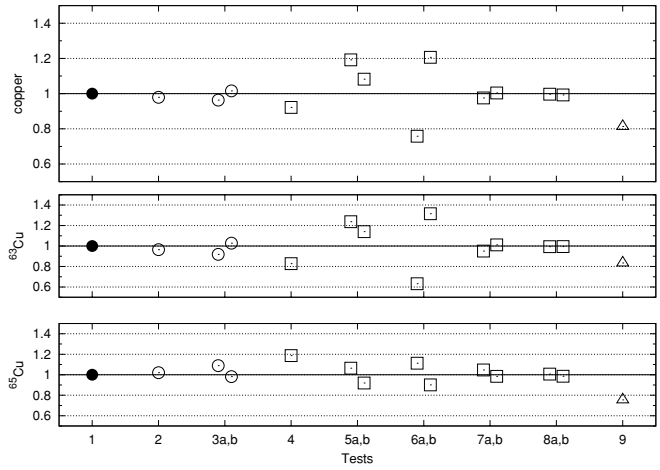

Figure 14. Production of copper (top) and of its stable isotopes ^{63}Cu (middle) and ^{65}Cu (bottom) are tested in our calculations for the 25 $M_{\odot}$ star with respect to different sources of uncertainty: (1) standard case (full circle); (2) results at the end of the constant temperature phase; (3a) and (3b) variation of the constant temperature phase of the C shell with lower and upper limits of $T_9 = 1.0$ and 1.1; (4) ^{22}Ne + α rates by NACRE; (5a) and (5b) limits of the rates by Heil et al. (2008b); (6a) and (6b) ^{63}Ni(n,γ)^{64}Ni MACS multiplied and divided by a factor of 2; (7a) and (7b) ^{63}Ni($\beta^-\nu$)^{63}Cu multiplied and divided by a factor of 3; (8a) and (8b) ^{64}Cu(n,γ)^{65}Cu MACS multiplied and divided by a factor of 2; (9) initial solar composition given by Lodders (2003) and Piersanti et al. (2007). Tests (2) and (3a), (3b) refer to model uncertainties (open circles), tests (4) and (8a), (8b) to nuclear uncertainties (open squares), and test (9) to the effect of using a different initial solar composition (open triangles).

provided by massive stars, respectively). For example, if [Cu/Fe] = −0.75 (see the lines in Figure 13) the primary component is 6%–9%. Considering contributions from AGB stars, SNe Ia and primary explosive yields from massive stars, only ∼ 20%–30% of solar copper can be reproduced. In our analysis, we support the scenario where the missing component is produced by the secondary weak *s*-process in massive stars.

Copper is one of the most produced elements by the *s*-process in core He-burning and in shell C-burning. With the new MACS by Alpizar-Vicente et al. (2008) and Heil et al. (2008b), the *s*-process yields of copper are enhanced with respect to calculations based on the MACS by Bao et al. (2000). The analysis of nuclear uncertainties discussed before opens the possibility for an even higher production (Figure 10). In Figure 14, we report another sample of tests, focused on copper nucleosynthesis: we consider the impact of model uncertainties (with and without the final temperature increase in the C shell, variation of the C shell temperature in the constant phase by 5%, see also Section 5), of nuclear uncertainties and of using different solar initial composition (figure caption for details). Note that more nuclear uncertainties are not addressed since they are marginal, e.g., ^{64}Cu($\beta^+\nu/\beta^-\nu$) decays and ^{65}Zn(n,γ). Figure 14 shows that nuclear uncertainties are more severe compared to stellar model uncertainties, in particular those of the ^{63}Ni(n,γ)^{64}Ni cross section and of the new MACS of ^{58}Fe, ^{59}Co, ^{64}Ni, and ^{63,65}Cu, especially at $kT = 90$ keV. The superposition of the different propagation effects yields an enhanced copper production even using the limits of these cross sections. The ^{63}Ni(n,γ)^{64}Ni MACS is crucial for the *s* abundance of ^{63}Cu. In the C shell, most of the ^{63}Cu built in the previous He core is depleted, and it is freshly produced as ^{63}Ni.

Using a more recent solar initial composition (e.g., Lodders 2003) instead of Anders & Grevesse (1989) in the calculations reduces by about 20% the copper *s* yields, affecting in particular ^{65}Cu. However, all the *s* elements heavier than copper are more significantly depleted (see Section 5 for a detailed discussion). For instance, this implies that the relative production factor of copper isotopes compared to *s*-only isotopes between Fe and Sr is higher, increasing also in this case the weak *s* component of copper. Summing up, these results are consistent with a stronger contribution of the weak *s*-process to solar copper than previously obtained. GCE calculations including *s* yields from a complete grid of stars are required in order to confirm this scenario. Note that, in the integrated abundance distribution over a complete massive star range by Chieffi & Limongi (2006), copper is the most produced *s* element beyond iron. We refer to a forthcoming paper for a more detailed analysis, where recent spectroscopic observations of copper are fully considered (e.g., Primas & Sobeck 2008).

6.2. Zinc

The weak *s* component of zinc is lower compared to other light trans-iron elements (Figure 11). Solar ^{64}Zn and possibly a significant part of ^{66}Zn (48% and 28% of solar zinc, respectively) are made by primary α-rich freeze-out in ν winds in massive stars (e.g., Woosley & Hoffman 1992). Bisterzo et al. (2005) proposed that most of the neutron-rich zinc isotopes (about half of solar zinc) are made by the weak *s*-process. As discussed in the previous section, the zinc abundance composition is affected by nuclear uncertainties, i.e., by the propagation of uncertainties in the MACS of ^{63,65}Cu in shell C-burning and by the expected revision of the old ^{66,67,68}Zn MACS. The weak *s*-process contribution is difficult to distinguish in spectroscopic observations of stars, because the explosive component is dominant at low metallicity (e.g., Bisterzo et al. 2005). Interestingly, both zinc and copper observations seem to show a peak at [Fe/H] ∼ −0.5, followed by a slight decrease with increasing metallicity due to the iron contribution from SNeIa (see Bisterzo et al. 2005, and reference therein for more details). Since for copper such a peak is related to the weak *s*-process, it is reasonable that the same argument may be applied to zinc. However, the observational uncertainties are too large to clearly identify the [Zn/Fe] peak at [Fe/H] ∼ −0.5, and to derive further conclusions for zinc.

6.3. Gallium

In our calculations, gallium is the most abundant element at the end of shell C-burning and, despite the large uncertainties previously discussed, we expect that most of the solar gallium is made by the *s*-process in massive stars. So far, gallium has been observed in only few stars at metallicities lower than solar: in the *r*-process-rich star HD221170 ([Fe/H] = −2.18; Ivans et al. 2006b), in the C-rich *r*-process star CS22892 − 052 ([Fe/H] = −3.1; Sneden et al. 2003, upper limit) and in the C-rich (*r* + *s*)-rich star CS29497 − 030 ([Fe/H] = −2.57; Ivans et al. 2005, 2006, upper limit). Gallium is also observed in other four metal poor stars (BD+80°245, G4 − 46, CS22966 − 043, and CS22941 − 012) by Ivans et al. (2003). However, the authors warn about the reliability of the GaI line (λ = 4172.0 Å) used for the analysis. Such a line is blended by Ti and Fe features and it could behave to some other element. For this reason, we will not consider those four stars in our analysis. In Figure 13, we plot the gallium observations together with observed copper abundances. In the stars CS22892 − 052 and HD221170 both elements are observed. Upper limits are not useful to derive any relevant conclusion, but the results for HD221170 are interesting since the observed Ga abundance at

[Fe/H] = −2.2 lies in the flat trend of copper abundance, and agrees with the observed copper in this star within 0.2 dex. This could imply that copper and gallium have a similar primary explosive component. More Ga observations are required in the future to constrain its nucleosynthesis origin as well as *s*-process predictions.

6.4. Germanium

Recently, Cowan et al. (2005) reported spectroscopic measurements of germanium for a sample of stars with low metallicity (−3 < [Fe/H] < −1.5), which show a flat trend of [Ge/Fe] = −0.79 on average. These observations are consistent with Ge abundance from HD126238 (Sneden et al. 1998), as shown in Figure 13.

As for copper, by using the same argument (Section 6.1) we may estimate the primary explosive component for germanium to be 5%–8%. The main *s* component provides about 12% according to Travaglio et al. (2004a). SNe Ia give a negligible contribution. Including the small contributions from AGB stars, SNe Ia and primary explosive yields from massive stars, about 20% of the solar germanium is explained. The weak *s*-process should reproduce the missing 80% (see also Sneden et al. 2008).

According to Figures 11 and 12, a correct evaluation of the weak *s* component of germanium depends on the ^{22}Ne + α rates, on the initial solar composition and on the MACS network, in particular in the Zn–Ga region. Recent (n,γ) measurements by Marganiec et al. (2009) of ^{74,76}Ge MACS imply higher *s*-process yields of Ge, improving the nucleosynthesis predictions. For ^{72,73}Ge there are only theoretical MACS values available, a situation that need to be improved by further experimental efforts. Independently of these uncertainties, Ge is one of the most abundant *s* elements at the end of the He core as well as at the end of the C shell, as shown in Figures 11 and 12. For this reason, we expect that the weak *s*-process is responsible for most of solar Ge. Germanium spectroscopic observations in the metallicity range −1.5 < [Fe/H] < 0 (where the Ge component made by the *s*-process in massive stars provides a significant contribution to the galactical chemical enrichment) are still missing. Such observations would be a strong constraint to test our predictions.

7. SPECIAL CASES

7.1. ^{36}S

The rare isotope ^{36}S contributes only 0.01% to the solar sulfur abundance. Whereas other stable sulfur isotopes are mainly made in hydrostatic/explosive neon and oxygen burning, ^{36}S is supposed to receive a relevant contribution from the weak *s*-process (e.g., Woosley et al. 2002; Mauersberger et al. 2004, and references therein).

Compared to Raiteri et al. (1991b), our predictions for the He core underproduce ^{36}S by about a factor of 3 (see Table 7). The main reason is the new ^{34}S(n,γ)^{35}S MACS from Reifarth et al. (2000), which is about 1 order of magnitude lower than previous rates. The use of the new MACS significantly reduces the production of ^{36}S via neutron capture from the lighter sulfur isotopes. As a consequence, the prevailing ^{36}S production channel in the weak *s*-process is ^{35}Cl(n,γ)^{36}Cl(n,p)^{36}S, where the initial ^{35}Cl is the main seed (Mauersberger et al. 2004). However, as discussed by Mauersberger et al. (2004), the solar abundances of Anders & Grevesse (1989) need to be updated by the new sulfur abundance of Palme & Beer (1993) and the new ratio ^{34}S/^{36}S = 288 ± 1 (Ding et al. 2001) and by using the chlorine abundance in Table 3 of Anders & Grevesse (1989) instead of the value given in Table 1 of that paper. In Table 10, we compare the sulfur and chlorine overabundances in the He core and at the end of the C shell with previous calculations (see also Tables 7 and 9, Model 1). The most affected isotope is ^{36}S, for which the overabundance increased by almost a factor of 2 due to the lower initial ^{36}S and the higher initial ^{35}Cl abundance. The new ^{37}Cl production factor decreased according to the new higher solar abundance. The new initial abundances for sulfur and chlorine do neither cause significant variations of the neutron exposure, nor of the isotope distribution beyond iron, since the corresponding increase of the *s* yields is less than 5%.

Table 10
Production Factors Using the New Solar Abundances for Sulfur and Chlorine (AG89 revised, see the text) in Comparison with Production Factors Obtained Using Anders & Grevesse 1989 (AG89)

X_i	AG89 Revised		AG89	
	He Core	C Shell	He Core	C Shell
S 32	0.5	0.3	0.5	0.3
S 33	1.1	1.7	1.1	1.7
S 34	1.5	1.9	1.5	1.8
S 36	57.3	77.1	28.5	41.1
Cl 35	0.2	0.3	0.2	0.5
Cl 37	46.7	47.0	64.4	64.8

Notes. The values refer to at the end of the He core and of the C shell (T_9 = 1.4). The nuclear network is that of Model 1.

7.2. ^{80}Kr

Updated GCE calculations predict that the main *s* component from AGB stars produce about 10% and 50% of the *s*-only isotopes ^{80}Kr and ^{82}Kr (Travaglio et al. 2004a). Explosive nucleosynthesis in massive stars contributes another 15% and 3% to ^{80}Kr and ^{82}Kr, respectively (Käppeler et al. 1989). Consequently, most of the ^{80}Kr and about half of ^{82}Kr in the solar system are coming from the weak *s*-process, with a production ratio ^{80}Kr/^{82}Kr ∼ 1.6. Since we are considering the *s*-process yields from only one star, we do not aim to reproduce this isotopic ratio. Nevertheless, we can derive a few important indications concerning the relevant nuclear and stellar model uncertainties.

Recent MACS measurements of ^{78}Se (Dillmann et al. 2006), ^{79,81}Br (Heil et al. 2008a), and ^{80,82}Kr (Mutti et al. 2005) improved the reliability of theoretical *s*-process predictions for the *s*-process abundances of ^{80}Kr and ^{82}Kr. As shown in Figure 10, the MACS of ^{79}Se is strongly affecting the ^{80}Kr abundance (e.g., Raiteri et al. 1991a, and references therein). Recently, Makinaga et al. (2009) confirmed that the present MACS of ^{79}Se is still uncertain by a factor of 2. The production of ^{80}Kr is also sensitive to the β-decay rate ^{79}Se(β^-)^{79}Br. See for example Figure 11 and relative discussion in Section 5, where in a test using the terrestrial β^- rate ^{80}Kr is completely destroyed in the C shell. Considering the present uncertainty of the ^{79}Se MACS and the ^{79}Se β-decay, the ^{80}Kr/^{82}Kr ratio in the He core and in the C shell may change within about a factor of 2. Furthermore, we showed that in shell C-burning the propagation effect along the *s* path due to uncertainties in the MACS of lighter isotopes represents another important source of uncertainty of ^{80,82}Kr (Figure 10).

A further uncertainty for the weak *s* production of ^{80}Kr is related to the stellar models, in particular to the temperature

behavior in the C shell. First, the average C-burning temperature and the average neutron density in the convective shell are modifying the ^{80}Kr/^{82}Kr ratio inherited from the He core phase. For example, variation of the C shell temperature by $\pm 5\%$ ($T_9 =$ 1 and 1.1, see also Figure 12, and 14 in case of copper), the respective ^{80}Kr/^{82}Kr ratios before the final temperature increase are 1.13 and 0.14. Second, the exposure to a final increase of temperature and neutron density at the end of the C-burning shell phase reduces the ^{80}Kr/^{82}Kr production ratio from 0.49 to 0.15 (Model 1, Table 9), compared to 2.14 obtained at the end of the He core (see Table 7). As discussed in Section 4, such a final neutron burst affects the *s*-process yields only if the convective C-burning shell is active in the last days before the SN explosion.

The low ^{80}Kr/^{82}Kr ratios in the C shell are difficult to reconcile with values of $\sim$ 1.6 needed to reproduce the weak *s*-process production ratio. On the other hand, as discussed in Section 1 a part of the SN ejecta is only affected by the He core phase, where a high ^{80}Kr/^{82}Kr ratio is obtained. Therefore, the ^{80}Kr/^{82}Kr ratio may be important for determining the mixture of material affected by C shell burning and by the He core phase only.

8. CONCLUSIONS AND FINAL REMARKS

In this paper, we present a new *s*-process analysis for a 25 $M_\odot$ star at solar metallicity. Post-processing calculations are provided for the convective He-burning core and for the convective C-burning shell in the light of updated nuclear reaction data.

We include most recent MACS measurements in the mass region between Fe and Sr, updating the compilation of Bao et al. (2000). The changes in the MACS of isotopes along the *s* path were found to cause a propagation effect to heavier isotopes, in particular when such cross sections are lower than $\sim$ 150 mbarn. At temperatures of $kT \sim 30$ keV, uncertainties of the new MACS are usually symmetric and lower than 10%, thus improving significantly the reliability of *s*-process nucleosynthesis calculations in the He core phase. However, a number of MACS in the Zn–Ga–Ge region and for Se need still to be re-measured, in order to improve further the reliability of *s*-process calculations in core He-burning. Furthermore, the final *s* yields and the *s*-process efficiency are also affected by the uncertainties of many charged particle reactions, such as ^{22}Ne + α and ^{12}C(α,γ)^{16}O. At C-burning temperatures ($kT \sim 90$ keV), the *s*-process calculations suffer from the generally larger uncertainties of the MACS data. At these higher temperatures, also most recent MACS measurements show larger (and often asymmetric) errors than at 30 keV. Also if such uncertainties do not significantly affect the neutron exposure or the number of neutrons captured per iron seed, they have a strong impact on the *s*-process distribution. The high neutron densities in the C-burning shell are activating several branchings along the *s* path. We showed that the uncertainties of the theoretical MACS of the unstable isotopes ^{63}Ni, ^{79}Se, and ^{85}Kr give rise to strong local propagation effects that need to be considered, whereas during He-burning such effects are smaller and covered by the impact of cross section uncertainties of the stable isotopes. Branching points are also affected by β-decay rates. The impact of their uncertainty depends on the branching nature. If the β-decay timescale is longer than the C shell timescale, the final yields are not or only marginally affected by the β-decay rate uncertainty (e.g., for copper nucleosynthesis see the case of ^{63}Ni(β^-)^{63}Cu, Section 6.1 and Figure 14). On the other hand, if the β-decay timescale is comparable with the neutron capture timescale, the uncertainty of the β-decay rate is relevant for the *s* yields depending on such branching (e.g., ^{79}Se(β^-)^{79}Br affects ^{80}Kr production).

Summing up, the *s*-process in the C shell is significantly affected by present uncertainties in the neutron capture network used in the calculations, and also β-decay rate uncertainties in branching points may affect the reliability of present *s*-process yields in massive stars. In general, production of *s*-process isotopes in the Fe–Cu region is less affected by uncertainties in nuclear data, compared to heavier species along the neutron capture path where more errors may be propagated.

Taking the nuclear uncertainties into account, we provide *s*-process abundances at the end of the He-burning core and of the C-burning shell, and discuss the consequences of a final temperature peak in the C shell. Previous works presented results with relevant differences concerning the C shell evolution in a 25 $M_\odot$ star, affecting the final *s*-process yields. For instance, if shell C-burning is active in the last days before the SN explosion, the higher temperature at the bottom of the shell causes a final neutron burst that can be significantly higher ($\sim$ few 10^{12} cm^{-3}) than the neutron density peak at C ignition ($\sim$ few 10^{11} cm^{-3}). The occurrence and the strength of such a neutron burst affects the *s* nucleosynthesis close to the branching points (e.g., by reducing the ^{80}Kr abundance), boosts the production of isotopes that are usually thought to be produced by the *r*-process (e.g., of ^{70}Zn), and increases the final *s* yields of As and Rb. Again, we obtain that lighter trans-iron elements as copper are weakly affected by uncertainty of the C shell evolution, and of the neutron density history.

More in general, model uncertainties not related to the nuclear physics network may have a significant impact on the weak *s*-process, and their relevance in different cases is not clear. Physics uncertainties are related for example on how treat convection in one-dimensional stellar models, where for instance mixing length theory (MLT) is used in most of one-dimensional stellar codes today (Kippenhahn & Weigert 1990). It is matter of debate what is the impact of one-dimensional model approximations on the *s*-process yields, in particular in the convective C shell (e.g., El Eid et al. 2009, and reference therein). Hydrodynamic simulations (e.g., Meakin & Arnett 2006; Herwig et al. 2006) indicate that mixing timescales and efficiencies in a small region located in particular at the bottom of the convection zone, are quantitatively not well described by MLT coefficients. Furthermore, starting from multi-dimensional simulations for the O shell and for the C shell, Meakin & Arnett (2006) showed that spherical symmetry is broken in pre-SN models. This is questioning the capability of one-dimensional stellar models to correctly simulate C shell nucleosynthesis, in particular in the last phases before SN explosion. Another question in one-dimensional models is the criteria to define the boundary of convective regions, for example choosing between the Ledoux and the Schwarzschild criteria (e.g., Langer et al. 1985). Also the overshooting parameter affects one-dimensional model *s*-process calculations (e.g., Langer et al. 1989; Costa et al. 2006), where more overshooting usually causes a higher *s*-process efficiency.

Explosive SN nucleosynthesis provides a significant contribution to many *s* isotopes (e.g., Rauscher et al. 2002; Tur et al. 2009) that needs to be considered with its large uncertainty. For example, see the discussion for copper production Section 6.1, and Pignatari et al. (2006) and Bisterzo et al. (2005). Starting from the solar abundance distribution, Käppeler et al. (1989) provided an empirical evaluation of such a contribution for the

s-only isotopes. However, only full stellar model calculations can provide a consistent evaluation for the explosive component of the *s* isotopes relative to the *s*-process component (e.g. Tur et al. 2009).

We also showed how *s*-process elements production is affected by the initial solar distribution. In particular, lower CNO abundances in recent solar abundance compilations (Lodders 2003; Piersanti et al. 2007; Lodders et al. 2009; Asplund et al. 2009) compared to Anders & Grevesse (1989) causes a decrease of ^{22}Ne available to produce neutrons (see also Tur et al. 2009). As a main consequence the *s*-process efficiency is reduced, in particular for *s* isotopes beyond Zn, whereas in the Fe–Cu region it is less sensitive to variations in the initial composition. Using solar composition by Lodders (2003; and re-evaluated according to Piersanti et al. 2007) we obtain a weak *s*-process distribution for a 25 $M_{\odot}$ star that seems more in agreement with the solar system distribution. This is just a qualitative remark, since we base this statement on one star only, and using a simplified one-zone model for the C shell nucleosynthesis. Further calculations are required, including also the explosive contribution.

Concluding, present stellar models are capable to analyze qualitatively the weak *s*-process. However, it is not clear at present if they are able to properly calculate a fully consistent *s*-process isotopic distribution, where many species (in particular the species affected by branching points) may be affected by nuclear physics uncertainties, and by convective–reactive conditions not properly considered by one-dimensional approximation.

Spectroscopic observations of copper and germanium at different metallicities provide important constraints for *s*-process calculations in massive stars. The new MACS measurements considered in our calculations result in an enhanced production of copper and germanium with respect to previous results, both in the He core and in the C shell. This supports the astrophysical scenario where the weak *s*-process is producing the missing 70%–80% of solar copper. In particular, a significant contribution to ^{63}Cu (69% of solar copper) is produced in the C shell by radiogenic decay of unstable ^{63}Ni. In this context, a direct measurement of the ^{63}Ni MACS is highly recommended in order to confirm and improve the reliability of our predictions. In our calculation, copper is the first element beyond iron that is mostly produced by the *s*-process. The *s*-process nucleosynthesis of this element is less affected by nuclear physics and stellar model uncertainties than heavier *s* elements. Therefore, theoretical *s*-process predictions for copper are generally more reliable than for heavier elements.

Recent spectroscopic studies of germanium at low metallicity started to shed some light on the nucleosynthesis origin of this element. In our scenario, about 80% of solar germanium is produced by the weak *s* process, but new MACS measurements are required for ^{66,67,68}Zn, ^{69,71}Ga, and ^{72,73}Ge in order to improve these predictions. Furthermore, future observations of Ge abundances in halo stars and in the metallicity range $-1.5 \lesssim$ [Fe/H] $\lesssim 0$ would be crucial to finally confirm this scenario.

Gallium is at the peak of the *s*-process production efficiency for a 25 $M_{\odot}$ star. Today the gallium abundance is clearly derived in only one star at [Fe/H] ~ -2.2, and it is in agreement with the copper abundance signature. More emphasis should be given to gallium in future spectroscopic studies at different metallicities, to confirm its *s*-process origin.

In contrast, zinc observations show marginal evidence of a weak *s*-process component. The only indication that we can derive from our simulations is that the *s* yields of zinc are lower than other trans-iron elements, i.e., copper, gallium, and germanium. However, within the still large nuclear uncertainties, a significant *s*-process contribution is obtained for the neutron-rich Zn isotopes (^{66,67,68}Zn).

Heavier *s* elements produced by the weak *s*-process are either spectroscopically not observed (e.g., As, Se) or receive a significant contribution from other processes (e.g., Sr, Y, and Zr from the main *s*-process in AGB stars, from the LEPP, and from the *r*-process), which covers their contribution from the weak *s*-process.

M.P. is supported by an EU Marie Curie grant MIRG-CT-2006-046520, and by NSF grants PHY 02-16783 and PHY-0822648 (JINA). R.G. and S.B. thank the Italian MIUR-PRIN06 project 2006022731_005. We thank Oscar Straniero for helpful discussions, concerning the solar abundance distribution.

REFERENCES

Aguilera, E. F., et al. 2006, Phys. Rev. C, 73, 064601
Aikawa, M., Arnould, M., Goriely, S., Jorissen, A., & Takahashi, K. 2005, A&A, 441, 1195
Alpizar-Vicente, A. M., et al. 2008, Phys. Rev. C, 77, 015806
Anders, E., & Grevesse, N. 1989, Geochim. Cosmochim. Acta, 53, 197
Angulo, C., et al. 1999, Nucl. Phys. A, 656, 3
Arlandini, C., Käppeler, F., Wisshak, K., Gallino, R., Lugaro, M., Busso, M., & Straniero, O. 1999, ApJ, 525, 886
Arnett, W. D. 1974, ApJ, 194, 373
Arnett, W. D., & Truran, J. W. 1969, ApJ, 157, 339
Arnett, W. D., & Wefel, J. P. 1978, ApJ, 224, L139
Asplund, M., Grevesse, N., & Sauval, A. J. 2005, in ASP Conf. Ser. 336, Cosmic Abundances as Records of Stellar Evolution and Nucleosynthesis, ed. T. G. Barnes, III & F. N. Bash (San Francisco, CA: ASP), 25
Asplund, M., Grevesse, N., Sauval, A. J., & Scott, P. 2009, ARA&A, 47, 481
Bao, Z. Y., Beer, H., Käppeler, F., Voss, F., Wisshak, K., & Rauscher, T. 2000, At. Data Nucl. Data Tables, 76, 70
Baraffe, I., El Eid, M. F., & Prantzos, N. 1992, A&A, 258, 357
Beer, H., Sedyshev, P. V., Rochow, W., Mohr, P., & Oberhummer, H. 2002, Nucl. Phys. A, 705, 239
Beer, H., Voss, F., & Winters, R. R. 1992a, ApJS, 80, 403
Beer, H., Walter, G., & Käppeler, F. 1992b, ApJ, 389, 784
Bihain, G., Israelian, G., Rebolo, R., Bonifacio, P., & Molaro, P. 2004, A&A, 423, 777
Bisterzo, S., Pompeia, L., Gallino, R., Pignatari, M., Cunha, K., Heger, A., & Smith, V. 2005, Nucl. Phys. A, 758, 284
Burbidge, E. M., Burbidge, G. R., Fowler, W. A., & Hoyle, F. 1957, Rev. Mod. Phys., 29, 547
Busso, M., & Gallino, R. 1985, A&A, 151, 205
Busso, M., Gallino, R., Lambert, D. L., Travaglio, C., & Smith, V. V. 2001, ApJ, 557, 802
Caughlan, G. R., & Fowler, W. A. 1988, At. Data Nucl. Data Tables, 40, 283
Caughlan, G. R., Fowler, W. A., Harris, M. J., & Zimmerman, B. A. 1985, At. Data Nucl. Data Tables, 32, 197
Chieffi, A., & Limongi, M. 2002, New Astron. Rev., 46, 459
Chieffi, A., & Limongi, M. 2006, in Proc. of Science, Int. Symp. on Nuclear Astrophysics—Nuclei in the Cosmos IX (Trieste: SISSA), PoS(NIC-IX)250
Chieffi, A., & Straniero, O. 1989, ApJS, 71, 47
Clayton, D. D. 1968, Principles of Stellar Evolution and Nucleosynthesis (New York: McGraw-Hill)
Cohen, J. G., Christlieb, N., McWilliam, A., Shectman, S., Thompson, I., Melendez, J., Wisotzki, L., & Reimers, D. 2008, ApJ, 672, 320
Coquard, L., Käppeler, , Dillmann, I., Wallner, A., Knie, K., & Kutschera, W. 2006, in Proc. of Science, Int. Symp. on Nuclear Astrophysics—Nuclei in the Cosmos IX (Trieste: SISSA), PoS(NIC-IX)274
Corvi, F., Fioni, G., Gunsing, F., Mutti, P., & Zanini, L. 2002, Nucl. Phys. A, 697, 581
Costa, V., Pumo, M. L., Bonanno, A., & Zappalà, R. A. 2006, A&A, 447, 641
Costa, V., Rayet, M., Zappalà, R. A., & Arnould, M. 2000, A&A, 358, L67
Couch, R. G., Schmiedekamp, A. B., & Arnett, W. D. 1974, ApJ, 190, 95
Cowan, J. J., et al. 2002, ApJ, 572, 861
Cowan, J. J., et al. 2005, ApJ, 627, 238

Dayras, R., Switkowski, Z. E., & Woosley, S. E. 1977, Nucl. Phys. A, 279, 70
de Smet, L., Wagemans, C., Goeminne, G., Wagemans, J., Heyse, J., & van Gils, J. 2005, Nucl. Phys. A, 758, 80
Dillmann, I., et al. 2006, in Proc. of Science, Int. Symp. on Nuclear Astrophysics—Nuclei in the Cosmos IX (Trieste: SISSA), PoS(NIC-IX)090
Ding, T., Valkiers, S., Kipphardt, H., De Bievre, P., Taylor, P. D. P., Gonfiantini, R., & Krouse, R. 2001, Geochim. Cosmochim. Acta, 65, 2433
El Eid, M. F., Meyer, B. S., & The, L.-S. 2004, ApJ, 611, 452
El Eid, M. F., The, L.-S., & Meyer, B. S. 2009, Space Sci. Rev., 147, 1
Farouqi, K., Kratz, K.-L., Mashonkina, L. I., Pfeiffer, B., Cowan, J. J., Thielemann, F.-K., & Truran, J. W. 2009, ApJ, 694, L49
Fuller, G. M., Fowler, W. A., & Newman, M. J. 1985, ApJ, 293, 1
Gallino, R., Arlandini, C., Busso, M., Lugaro, M., Travaglio, C., Straniero, O., Chieffi, A., & Limongi, M. 1998, ApJ, 497, 388
Goeminne, G., Wagemans, C., Wagemans, J., Serot, O., Loiselet, M., & Gaelens, M. 2000, Nucl. Phys. A, 678, 11
Guber, K. H., Koehler, P. E., Derrien, H., Valentine, T. E., Leal, L. C., Sayer, R. O., & Rauscher, T. 2003, Phys. Rev. C, 67, 062802
Heil, M., Juseviciute, A., Käppeler, F., Gallino, R., Pignatari, M., & Uberseder, E. 2009, PASA, 26, 243
Heil, M., Käppeler, F., Uberseder, E., Gallino, R., Bisterzo, S., & Pignatari, M. 2008a, Phys. Rev. C, 78, 025802
Heil, M., Käppeler, F., Uberseder, E., Gallino, R., & Pignatari, M. 2007, Progr. Part. Nucl. Phys., 59, 174
Heil, M., Käppeler, F., Uberseder, E., Gallino, R., & Pignatari, M. 2008b, Phys. Rev. C, 77, 015808
Heil, M., Plag, R., Gallino, R., Juseviciute, A., Käppeler, F., & Mengoni, A. 2005, in AIP Conf. Proc. 769, Int. Conf. on Nuclear Data for Science and Technology, ed. R. C. Haight et al. (Melville, NY: AIP), 1362
Herwig, F., Freytag, B., Hueckstaedt, R. M., & Timmes, F. X. 2006, ApJ, 642, 1057
Hirschi, R., Meynet, G., & Maeder, A. 2004, A&A, 425, 649
Hoeflich, P., Wheeler, J. C., & Thielemann, F. K. 1998, ApJ, 495, 617
Honda, S., Aoki, W., Kajino, T., Ando, H., Beers, T. C., Izumiura, H., Sadakane, K., & Takada Hidai, M. 2004, ApJ, 607, 474
Imbriani, G., Limongi, M., Gialanella, L., Terrasi, F., Straniero, O., & Chieffi, A. 2001, ApJ, 558, 903
Ivans, I. I., Bisterzo, S., & Gallino, R. 2006, Mem. Soc. Astron. Italiana, 77, 979
Ivans, I. I., Sneden, C., Gallino, R., Cowan, J. J., & Preston, G. W. 2005, ApJ, 627, L145
Ivans, I. I., Sneden, C., James, C. R., Preston, G. W., Fulbright, J. P., Höflich, P. A., Carney, B. W., & Wheeler, J. C. 2003, ApJ, 592, 906
Iwamoto, K., Brachwitz, F., Nomoto, K., Kishimoto, N., Umeda, H., Hix, W. R., & Thielemann, F.-K. 1999, ApJS, 125, 439
Jaeger, M., Kunz, R., Mayer, A., Hammer, J. W., Staudt, G., Kratz, K. L., & Pfeiffer, B. 2001, Phys. Rev. Lett., 87, 202501
Johnson, J. A., & Bolte, M. 2004, ApJ, 605, 462
Jonsell, K., Barklem, P. S., Gustafsson, B., Christlieb, N., Hill, V., Beers, T. C., & Holmberg, J. 2006, A&A, 451, 651
Käppeler, F., Beer, H., & Wisshak, K. 1989, Rep. Prog. Phys., 52, 945
Käppeler, F., et al. 1994, ApJ, 437, 396
Karakas, A. I., Lugaro, M. A., Wiescher, M., Görres, J., & Ugalde, C. 2006, ApJ, 643, 471
Kippenhahn, R., & Weigert, A. 1990, Sky Telesc., 80, 504
Klay, N., & Käppeler, F. 1988, Phys. Rev. C, 38, 295
Koehler, P. E., Kavanagh, R. W., Vogelaar, R. B., Gledenov, Y. M., & Popov, Y. P. 1997, Phys. Rev. C, 56, 1138
Koehler, P. E., & O'Brien, H. A. 1989, Phys. Rev. C, 39, 1655
Kratz, K.-L., Farouqi, K., Mashonkina, L. I., & Pfeiffer, B. 2008, New Astron. Rev., 52, 390
Lai, D. K., Bolte, M., Johnson, J. A., Lucatello, S., Heger, A., & Woosley, S. E. 2008, ApJ, 681, 1524
Lamb, S. A., Howard, W. M., Truran, J. W., & Iben, I., Jr. 1977, ApJ, 217, 213
Langanke, K., & Martínez-Pinedo, G. 2000, Nucl. Phys. A, 673, 481
Langer, N., Arcoragi, J.-P., & Arnould, M. 1989, A&A, 210, 187
Langer, N., El Eid, M. F., & Fricke, K. J. 1985, A&A, 145, 179
Limongi, M., Straniero, O., & Chieffi, A. 2000, ApJS, 129, 625
Lodders, K. 2003, ApJ, 591, 1220
Lodders, K., Palme, H., & Gail, H. 2009, arXiv:0901.1149
Lugaro, M., Davis, A. M., Gallino, R., Pellin, M. J., Straniero, O., & Käppeler, F. 2003, ApJ, 593, 486
Makinaga, A., et al. 2009, Phys. Rev. C, 79, 025801
Marganiec, J., Dillmann, I., Domingo Pardo, C., Käppeler, F., Gallino, R., Pignatari, M., & Grabmayr, P. 2009, Phys. Rev. C, 79, 065802
Masseron, T., et al. 2006, A&A, 455, 1059
Matteucci, F., Raiteri, C. M., Busso, M., Gallino, R., & Gratton, R. 1993, A&A, 272, 421
Mauersberger, R., Ott, U., Henkel, C., Cernicharo, J., & Gallino, R. 2004, A&A, 426, 219
Meakin, C. A., & Arnett, D. 2006, ApJ, 637, L53
Meyer, B. S., Clayton, D. D., & The, L.-S. 2000, ApJ, 540, L49
Mishenina, T. V., Kovtyukh, V. V., Soubiran, C., Travaglio, C., & Busso, M. 2002, A&A, 396, 189
Mutti, P., Beer, H., Brusegan, A., Corvi, F., & Gallino, R. 2005, in AIP Conf. Proc. 769, Int. Conf. on Nuclear Data for Science and Technology, ed. R. C. Haight et al. (Melville, NY: AIP), 1327
Nassar, H., et al. 2005, Phys. Rev. Lett., 94, 092504
Neuberger, D. 1991, Diploma thesis, Univ. Karlsruhe
Nomoto, K., & Hashimoto, M. 1988, Phys. Rep., 163, 13
Palme, H., & Beer, H. 1993, in Landolt Börnstein Group VI, Astronomy and Astrophysics 2A, ed. H. H. Voigt (Berlin: Springer), 196
Peters, J. G. 1968, ApJ, 154, 225
Piersanti, L., Straniero, O., & Cristallo, S. 2007, A&A, 462, 1051
Pignatari, M., & Gallino, R. 2008, in AIP Conf. Proc. 990, First Stars III, ed. B. W. O'Shea & A. Heger (Melville, NY: AIP), 336
Pignatari, M., Gallino, R., Heger, A., Woosley, S. E., & Käppeler, F. 2006, in ESO Astrophys. Symp., Chemical Abundances and Mixing in Stars in the Milky Way and its Satellites, ed. S. Randich & L. Pasquini (Berlin: Springer-Verlag), 320
Pignatari, M., Gallino, R., Meynet, G., Hirschi, R., Herwig, F., & Wiescher, M. 2008, ApJ, 687, L95
Prantzos, N., Hashimoto, M., & Nomoto, K. 1990, A&A, 234, 211
Primas, F., & Sobeck, J. 2008, in AIP Conf. Proc. 1001, Evolution and Nucleosynthesis in AGB Stars, ed. R. Guandalini, S. Palmerini, & M. Busso (Melville, NY: AIP), 230
Qian, Y.-Z., & Wasserburg, G. J. 2008, ApJ, 687, 272
Raiteri, C. M., Busso, M., Picchio, G., & Gallino, R. 1991a, ApJ, 371, 665
Raiteri, C. M., Busso, M., Picchio, G., Gallino, R., & Pulone, L. 1991b, ApJ, 367, 228
Raiteri, C. M., Gallino, R., & Busso, M. 1992, ApJ, 387, 263
Raiteri, C. M., Gallino, R., Busso, M., Neuberger, D., & Käppeler, F. 1993, ApJ, 419, 207
Rauscher, T., Heger, A., Hoffman, R. D., & Woosley, S. E. 2002, ApJ, 576, 323
Rauscher, T., & Thielemann, F.-K. 2000, At. Data Nucl. Data Tables, 75, 1
Rayet, M., & Hashimoto, M.-a. 2000, A&A, 354, 740
Reifarth, R., Schwarz, K., & Käppeler, F. 2000, ApJ, 528, 573
Romano, D., & Matteucci, F. 2007, MNRAS, 378, L59
Schatz, H., Käppeler, F., Koehler, P. E., Wiescher, M., & Trautvetter, H.-P. 1993, ApJ, 413, 750
Skelton, R. T., Kavanagh, R. W., & Sargood, D. G. 1987, Phys. Rev. C, 35, 45
Sneden, C., Cowan, J. J., Burris, D. L., & Truran, J. W. 1998, ApJ, 496, 235
Sneden, C., Cowan, J. J., & Gallino, R. 2008, ARA&A, 46, 241
Sneden, C., & Crocker, D. A. 1988, ApJ, 335, 406
Sneden, C., Gratton, R. G., & Crocker, D. A. 1991, A&A, 246, 354
Sneden, C., et al. 2003, ApJ, 591, 936
Suda, T., et al. 2008, PASJ, 60, 1159
Takahashi, K., & Yokoi, K. 1987, At. Data Nucl. Data Tables, 36, 375
The, L.-S., El Eid, M. F., & Meyer, B. S. 2007, ApJ, 655, 1058
Thielemann, F. K., & Arnett, W. D. 1985, ApJ, 295, 604
Timmes, F. X., Woosley, S. E., & Weaver, T. A. 1995, ApJS, 98, 617
Tinsley, B. M. 1980, Fundam. Cosm. Phys., 5, 287
Tominaga, N., Umeda, H., & Nomoto, K. 2007, ApJ, 660, 516
Travaglio, C., Gallino, R., Arnone, E., Cowan, J., Jordan, F., & Sneden, C. 2004a, ApJ, 601, 864
Travaglio, C., Hillebrandt, W., & Reinecke, M. 2005, A&A, 443, 1007
Travaglio, C., Hillebrandt, W., Reinecke, M., & Thielemann, F.-K. 2004b, A&A, 425, 1029
Tur, C., Heger, A., & Austin, S. M. 2009, ApJ, 702, 1068
Ugalde, C. 2008, in Proc. of Science, 10th Symp. on Nuclei in the Cosmos (Trieste: SISSA), PoS(NIC X)038
Utku, S., et al. 1998, Phys. Rev. C, 57, 2731
Wagemans, C., Druyts, S., & Barthélémy, R. 1995, in AIP Conf. Proc. 327, Nuclei in the Cosmos III, ed. M. Busso, C. M. Raiteri, & R. Gallino (Melville, NY: AIP), 169
Wagoner, R. V. 1969, ApJS, 18, 247
Ward, R. A., Newman, M. J., & Clayton, D. D. 1976, ApJS, 31, 33
Westin, J., Sneden, C., Gustafsson, B., & Cowan, J. J. 2000, ApJ, 530, 783
Woosley, S. E., & Heger, A. 2007, Phys. Rep., 442, 269
Woosley, S. E., Heger, A., & Weaver, T. A. 2002, Rev. Mod. Phys., 74, 1015
Woosley, S. E., & Hoffman, R. D. 1992, ApJ, 395, 202
Woosley, S. E., & Weaver, T. A. 1995, ApJS, 101, 181